Journal of Marine Science and Engineering

MDPI

Article

Disturbance-Estimation-Driven Time-Varying Bandwidth Active Disturbance Rejection Control for Shipboard Boom Cranes

Yuebang He [1], Long Chen [2], Tianlei Wang [2,*], Jianyi Yan [2,*], Xiaodong Wang [3], Weizhuo Huang [1], Chuanbin Xu [4] and Xiangjun He [5]

[1] School of Mechanical and Automation Engineering, Wuyi University, Jiangmen 529020, China; heyuebang@foxmail.com (Y.H.); 18902290927@163.com (W.H.)
[2] School of Electronic and Information Engineering, Wuyi University, Jiangmen 529020, China; longchen0915@126.com
[3] Guangdong Kejie Technology Co., Ltd., Jiangmen 529099, China; 19129231545@163.com
[4] Shenzhen Sinovo Electric Technologies Co., Ltd., Shenzhen 518000, China; wang1689gb@163.com
[5] Guangdong Tiandi Intelligent Equipment Co., Ltd., Jiangmen 529400, China; linkelim@163.com
* Correspondence: tianlei.wang@aliyun.com (T.W.); yanjianyi@wyu.edu.cn (J.Y.)

Abstract

Shipboard boom cranes require accurate positioning and load-swing suppression despite underactuation and disturbance coupling. This study investigates a disturbance-estimation-driven time-varying bandwidth active disturbance rejection control (TVB-ADRC) framework. A nominal differential-flatness mapping, a fourth-order derivative observer, and a leakage disturbance observer are combined with bounded, smoothed observer/controller bandwidth scheduling. Conditional convergence is established for an ideal flat-output error model, together with an ultimate error bound for a bounded, nonvanishing residual. This analysis does not constitute an unconditional stability proof for the complete nonlinear proportional-derivative-augmented implementation. Six simulation cases are compared using explicitly defined finite-window performance indices. The complete TVB-ADRC configuration achieves faster actuated-state regulation in several cases than the fixed-bandwidth ADRC and active-swing-control configurations, although it does not minimize every swing metric. A laboratory positioning experiment uses prescribed sinusoidal excitation to represent periodic wave disturbance and reports a peak swing of 2.79 degrees. This laboratory excitation is distinct from the stochastic wave signal used in simulation. The laboratory input-level interpretation uses an inferred mass-moment estimate rather than an independently measured value, and the comparisons do not isolate the independent contribution of bandwidth scheduling.

Keywords: active disturbance rejection control; anti-swing control; differential flatness; disturbance observer; shipboard boom crane; time-varying bandwidth

Check for updates

Academic Editor: Weicheng Cui

Received: 9 October 2026
Revised: 27 October 2026
Accepted: 29 October 2026
Published: 4 November 2026

Copyright: © 2026 by the authors. Licensee MDPI, Basel, Switzerland. This article is an open access article distributed under the terms and conditions of the Creative Commons Attribution (CC BY) license.

1. Introduction

Shipboard boom cranes are used for offshore replenishment, construction, and cargo transfer. Their underactuated load swing couples to luffing, hoisting, and vessel motion. Reviews of crane dynamics and control describe the resulting positioning and anti-swing challenges [1,2]. Offshore studies explicitly treating vessel motion further motivate disturbance-aware control [3,4]. The present work addresses a planar luffing–hoisting subsystem rather than full three-dimensional vessel–crane dynamics.

Anti-swing strategies include open-loop trajectory design and closed-loop feedback. Input shaping [5] and optimal or polynomial planning [6,7] reduce nominal excitation,

whereas feedback methods address uncertainty during motion. Coupling-based adaptive control [8], adaptive fuzzy control [9], and state-constrained neural control [10,11] address different forms of tracking and uncertainty. These methods are not interchangeable, and no claim is made that feedback or adaptive anti-swing control is absent from the literature.

For shipboard cranes, coordinate transformations account for roll [3], nonlinear stabilizing control treats roll and heave [4], and dynamic feedback avoids direct velocity measurements [12]. Input dead zones [13], output hysteresis [14], and deck-relative stabilization [15] introduce further practical issues. These results establish relevant moving-base control capabilities; the narrower question examined here is how a disturbance-estimate scheduling signal can be combined with flat-output derivative reconstruction.

Active disturbance rejection control (ADRC) treats uncertain dynamics and external inputs as a total disturbance estimated for compensation. Han [16] describes the extended-state-observer (ESO) framework, while Gao [17] develops bandwidth-based parameterization. In offshore cranes, Lu et al. [18] use nonlinear swing-coupling feedback, and Li et al. [19] combine differential flatness with ADRC. The fixed gains used for the latter comparator in this study are reported explicitly. Increasing bandwidth can improve nominal response but can also amplify measurement noise; a fixed setting therefore represents a tuning trade-off rather than a universal deficiency of ADRC.

Observer design and adaptation also extend beyond fixed-bandwidth ADRC. Finite-time disturbance estimation has been applied to offshore cranes [20], and fuzzy adaptive linear ADRC has been studied in visual servoing [21]. Phan et al. [22] combine an enhanced super-twisting ESO with adaptive terminal sliding-mode control for an electronic throttle. The work of Ortiz Hernández et al. [23] applies ADRC to inclined-surface Mecanum-wheel motion, addressing gravity and slippage. These are related observer-based robustness strategies, not evidence that the same two-channel flatness-based scheduling architecture has already been tested on a shipboard crane. Conversely, this paper does not claim to originate adaptive observation or variable-bandwidth ADRC in general.

The specific design explored here uses a leakage disturbance estimate both for compensation and for scheduling four bounded bandwidth states. It differs from an augmented ESO because derivative reconstruction and disturbance estimation are represented separately, although they share the same output residual and are not statistically independent. It differs from the cited throttle controller in its control law, scheduling mechanism, and underactuated application. The inclined-robot paper supports the relevance of ADRC under motion-dependent disturbances but is not used as evidence for a particular bandwidth update law. The available comparisons cannot establish superiority over all adaptive-bandwidth methods.

The proposed implementation maps nominal crane motion to two flat-output channels, reconstructs their derivative chains, and uses estimated disturbance magnitude to schedule observer and controller gains through smooth bounded updates. This is a tunable design mechanism, not a guaranteed improvement in every operating condition. In particular, bounded scheduling cannot remove arbitrary estimation bias or certify noise robustness.

The contributions and evidence are as follows:

1. A two-channel controller architecture combines flat-output derivative reconstruction, leakage disturbance estimation, and bounded observer/controller bandwidth scheduling. The scheduling equations and their implementation limits are made explicit.
2. A conditional virtual-error analysis distinguishes asymptotic convergence under vanishing residuals from ultimate bounds under nonvanishing residuals. The scope excludes an unproved full nonlinear PD-loop stability claim.
3. Six archived simulation records are reassessed with reproducible metrics, together with a laboratory-response summary. The results compare complete configura-

tions; a structure-matched scheduling ablation and quantified noise/delay tests remain unavailable.

2. Problem Formulation

2.1. Mathematical Model of the Shipboard Boom Crane

Figure 1 shows the planar crane geometry. Here, m_p is the payload mass, P_L is the equivalent boom length, J is the equivalent boom inertia, and $m_d = m_b d_b$ is the boom mass–center-of-mass-distance product (unit kg m), not a mass. The angle convention is specified by the coordinate change below and by the load-position geometry in Section 3.1. All model angles are in radians; response plots use degrees.

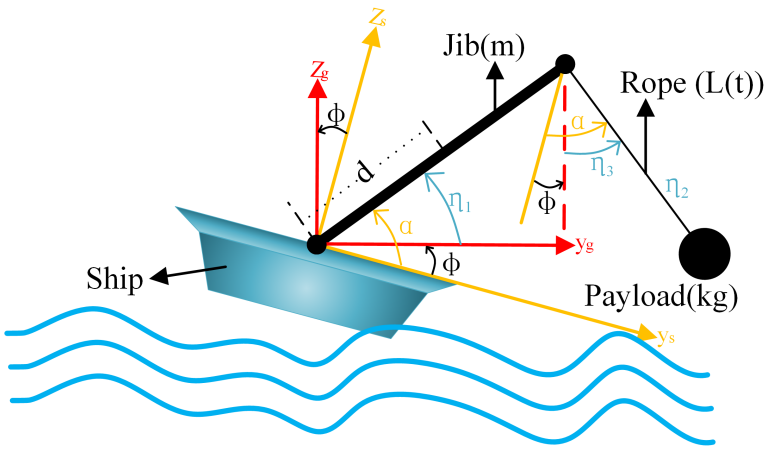


Figure 1. Schematic illustration of the shipboard boom crane.

The equations governing the planar motion of the load are derived as follows [3]:

$$M(q)\ddot{q} + C(q,\dot{q})\dot{q} + G(q) = u + \mathbf{r}_q. \tag{1}$$

where $q = [\alpha\ l\ \theta]^T \in \mathbb{R}^3$ is the state vector, $M(q) \in \mathbb{R}^{3\times3}$ and $C(q,\dot{q}) \in \mathbb{R}^{3\times3}$ denote the inertia matrix and the centripetal–Coriolis matrix, respectively, $G(q) \in \mathbb{R}^3$ represents the gravity vector, and $u \in \mathbb{R}^3$ and $\mathbf{r}_q \in \mathbb{R}^3$ denote the control-input vector and the disturbance vector, respectively. All elements contained in the above matrices and vectors are given as follows:

$$M(q) = \begin{bmatrix} J + m_p P_L^2 & -m_p P_L \cos(\theta-\alpha) & m_p P_L l \sin(\theta-\alpha) \\ -m_p P_L \cos(\theta-\alpha) & m_p & 0 \\ m_p P_L l \sin(\theta-\alpha) & 0 & m_p l^2 \end{bmatrix}. \tag{2}$$

$$C(q,\dot{q}) = \begin{bmatrix} 0 & m_p P_L \sin(\theta-\alpha)\dot{\theta} & c_{13}^q \\ -m_p P_L \sin(\theta-\alpha)\dot{\alpha} & 0 & -m_p l\dot{\theta} \\ -m_p P_L l \cos(\theta-\alpha)\dot{\alpha} & m_p l\dot{\theta} & m_p l\dot{l} \end{bmatrix}. \tag{3}$$

$$G(q) = \begin{bmatrix} (m_p P_L + m_d)(g + \ddot{h})\cos(\alpha-\varphi) \\ -m_p(g+\ddot{h})\cos(\theta-\varphi) \\ m_p l(g+\ddot{h})\sin(\theta-\varphi) \end{bmatrix}. \tag{4}$$

$$\begin{aligned} &\mathbf{r}_q = \mathbf{r}_\eta + M(q)b\ddot{\varphi} + C(q,\dot{q})\dot{q} - C(\eta,\dot{\eta})\dot{\eta}, \\ &b = [1\ 0\ 1]^T, \qquad q = \eta + b\varphi. \end{aligned} \tag{5}$$

In this notation $\varphi(t)$ is the prescribed angular offset, and $h(t)$ is the vertical base displacement. The identity (5) defines the original-coordinate residual consistently with the transformed equation, since $M(q) = M(\eta)$ and $G(q) = G(\eta)$ under the stated substitution.

It replaces undefined disturbance-component indices; it is not a vessel-response model. Here, $c_{13}^{q} = m_p P_L[\sin(\theta-\alpha)\dot{l} + l\cos(\theta-\alpha)\dot{\theta}]$. The swing-damping coefficient is $c_\theta > 0$ (unit N m s/rad).

$$\eta = \begin{bmatrix} \eta_1 & \eta_2 & \eta_3 \end{bmatrix}^T = \begin{bmatrix} \alpha - \varphi & l & \theta - \varphi \end{bmatrix}^T. \tag{6}$$

With the transformation (6) and the residual identity (5), the model is written as

$$M(\eta)\ddot{\eta} + C(\eta,\dot{\eta})\dot{\eta} + G(\eta) = u + \mathbf{r}_\eta. \tag{7}$$

$$M(\eta) = \begin{bmatrix} J + m_p P_L^2 & -m_p P_L C_{1-3} & -m_p P_L \eta_2 S_{1-3} \\ -m_p P_L C_{1-3} & m_p & 0 \\ -m_p P_L \eta_2 S_{1-3} & 0 & m_p \eta_2^2 \end{bmatrix}. \tag{8}$$

$$C = \begin{bmatrix} 0 & -m_p P_L S_{1-3}\dot{\eta}_3 & c_{13} \\ m_p P_L S_{1-3}\dot{\eta}_1 & 0 & -m_p \eta_2 \dot{\eta}_3 \\ -m_p P_L \eta_2 C_{1-3}\dot{\eta}_1 & m_p \eta_2 \dot{\eta}_3 & m_p \eta_2 \dot{\eta}_2 \end{bmatrix}. \tag{9}$$

$$G = \begin{bmatrix} G_1 & -m_p(g+\ddot{h})C_3 & m_p \eta_2 (g+\ddot{h}) S_3 \end{bmatrix}^T. \tag{10}$$

$$\mathbf{r}_\eta = \begin{bmatrix} 0 & 0 & -c_\theta \dot{\eta}_3 \end{bmatrix}^T + \mathbf{w}(t). \tag{11}$$

$$u = \begin{bmatrix} M_c & F_l & 0 \end{bmatrix}^T. \tag{12}$$

Here, $M(\eta)$ and $C(\eta,\dot{\eta})$ are the transformed inertia and centripetal–Coriolis matrices, $G(\eta)$ is the transformed gravity vector, $u = [M_c\ F_l\ 0]^T$ is the control-input vector, and $\mathbf{r}_\eta$ collects the transformed disturbance terms. The trigonometric shorthand is $C_1 = \cos\eta_1$, $S_1 = \sin\eta_1$, $C_{1-3} = \cos(\eta_1 - \eta_3)$, $S_{1-3} = \sin(\eta_1 - \eta_3)$, $C_3 = \cos\eta_3$, and $S_3 = \sin\eta_3$. The remaining coefficients and generalized disturbance are defined by

$$\begin{aligned} c_{13} &= m_p P_L(-S_{1-3}\dot{\eta}_2 + \eta_2 C_{1-3}\dot{\eta}_3), \\ G_1 &= (m_p P_L + m_d)(g+\ddot{h})C_1. \end{aligned} \tag{13}$$

Here, $\mathbf{w}(t)$ collects any additional generalized inputs, including prescribed motion and forcing not explicitly represented on the left-hand side. Its components have torque, force, and torque units, respectively. The archived plant evaluates the displayed matrices with $\ddot{h} = 0$ and a separate disturbance input; a wave-to-vessel roll/heave transfer function is not available. For $m_p > 0$, $J > 0$, and $\eta_2 > 0$, the leading principal minors are positive, and $\det M = J m_p^2 \eta_2^2 > 0$. The matrices satisfy $\dot{M} - C - C^T = 0$, verified symbolically using their displayed entries, and hence

$$x^T\left[\frac{1}{2}\dot{M} - C\right]x = 0, \qquad \forall x \in \mathbb{R}^3. \tag{14}$$

2.2. Control Objectives and Reasonable Assumptions

In the earth-fixed coordinate system, the objective is to transport the load from its initial position to a desired position while eliminating residual load swing. For the transformed shipboard boom crane system described by Equation (7), the goal is to design a suitable controller u to achieve the following control objectives:

$$\begin{bmatrix} \eta_1 & \eta_2 & \eta_3 & \dot{\eta}_1 & \dot{\eta}_2 & \dot{\eta}_3 \end{bmatrix}^T = \begin{bmatrix} \eta_{1d} & \eta_{2d} & 0 & 0 & 0 & 0 \end{bmatrix}^T. \tag{15}$$

where η_{1d} and η_{2d} denote the desired transformed luffing coordinate and cable length, respectively; through (6), the desired physical boom angle is $\alpha_d(t) = \eta_{1d} + \varphi(t)$, and the desired physical cable length is $l_d = \eta_{2d}$. A three-degree-of-freedom rotary crane is considered as the research platform. To retain the essential dynamics while keeping the analysis tractable, the following modeling assumptions are adopted:

1. During transportation, both the luffing angle and the load swing angle are confined within the range $(-90°, 90°)$.
2. The initial and desired cable lengths are within reasonable bounds: $l_{\min} \le l(0), l_d \le l_{\max}$, where $l_{\max}$ is the upper bound of the cable length in practical applications.

3. Time-Varying Bandwidth ADRC Design

3.1. Differential Flatness Analysis and Coordinate Mapping

Given the underactuated, strongly coupled nature of the shipboard boom crane system and its susceptibility to sea-state disturbances, an equivalent description of the system is first established in the flat-output space. The key concept of differential flatness theory is to construct a set of flat outputs such that all state variables and control inputs of the system can be explicitly expressed in terms of these outputs and their finite-order derivatives. Based on the geometric relationship of load motion, the Cartesian coordinates of the load, denoted as x_p and z_p, are selected as candidate flat outputs, where x_p represents the horizontal position coordinate of the load, and z_p represents the vertical position coordinate. From the system configuration, we obtain the following:

$$x_p = P_L C_1 + \eta_2 S_3, \qquad z_p = P_L S_1 - \eta_2 C_3. \tag{16}$$

Differentiating Equation (16) twice with respect to time and combining with the original system dynamic equations yields the following:

$$\ddot{x}_p C_3 + \ddot{z}_p S_3 = -P_L C_{1-3} \dot{\eta}_1^2 - P_L S_{1-3} \ddot{\eta}_1 + 2\dot{\eta}_2 \dot{\eta}_3 + \eta_2 \ddot{\eta}_3. \tag{17}$$

For the nominal undamped subsystem, with $\ddot{h} = 0$ and no extra swing-channel generalized input, the third mechanical equation reduces this identity to

$$\ddot{x}_p C_3 + \left(g + \ddot{z}_p\right) S_3 = 0. \tag{18}$$

Provided $\ddot{x}_p^2 + (g + \ddot{z}_p)^2 > 0$, a continuous admissible branch gives

$$\eta_3 = \operatorname{atan2}\left(-\ddot{x}_p,\, g + \ddot{z}_p\right). \tag{19}$$

From Equation (16), we can first rearrange as follows:

$$x_p - P_L C_1 = \eta_2 S_3, \qquad P_L S_1 - z_p = \eta_2 C_3. \tag{20}$$

Dividing the two equations yields the following:

$$\tan \eta_3 = \frac{x_p - P_L C_1}{P_L S_1 - z_p}. \tag{21}$$

Then, combining Equations (16), (18) and (20) and eliminating the coupling terms between l and θ, we obtain the following:

$$\ddot{x}_p z_p - x_p \ddot{z}_p - x_p g = P_L\left[\ddot{x}_p S_1 - \left(g + \ddot{z}_p\right) C_1\right]. \tag{22}$$

Further applying trigonometric identities, the transformed luffing coordinate η_1 can be solved as follows:

$$\eta_1 = \arccos\left(-\frac{\ddot{x}_p z_p - x_p \ddot{z}_p - x_p g}{P_L \sqrt{\ddot{x}_p^2 + \left(g + \ddot{z}_p\right)^2}}\right) + \operatorname{atan2}\left(-\ddot{x}_p,\, g + \ddot{z}_p\right). \tag{23}$$

Finally, within the normal operating domain $l > 0$, the cable length can be directly reconstructed from the geometric relationship:

$$\eta_2 = \frac{P_L \sin \eta_1 - z_p}{\cos \eta_3}. \tag{24}$$

These relations provide a local flatness reconstruction for the nominal undamped model [19]. The branch of the inverse trigonometric functions must be fixed consistently with the initial configuration; $\cos\eta_3 \neq 0$, a positive cable length, and an arccos argument strictly inside $(-1, 1)$ avoid singular boundaries. Damping, additional swing forcing, and imperfect base-motion compensation invalidate the exact nominal pendulum identity unless included as model residuals. They are therefore not silently removed from the implemented plant or claimed to preserve exact flatness of every disturbed trajectory.

The desired limits of the transformed coordinates are

$$\eta_1(t) \to \eta_{1d}, \qquad \eta_2(t) \to \eta_{2d}, \qquad \eta_3(t) \to 0.$$

The desired reference trajectories for the flat outputs can be constructed from Equation (16). At this point, the original system control problem has been transformed into a trajectory tracking problem in the flat-output space, providing a unified coordinate basis for subsequent controller design.

3.2. Observer, Bandwidth Scheduling, and Control Law

Section 3.1 reformulates the original underactuated system in the flat-output space into a standard form suitable for controller design. The proposed time-varying active disturbance rejection control law is then constructed in the flat-output coordinates. It comprises reference-trajectory generation, state-derivative reconstruction, lumped-disturbance estimation, time-varying bandwidth scheduling, and physical-input mapping, which together provide active anti-swing control within a unified framework. Figure 2 summarizes the resulting closed-loop architecture and its information flow.

The measured crane states are mapped back to the flat-output coordinates and reconstructed by the fourth-order derivative observer. In parallel, the separate leakage disturbance observer estimates the lumped channel disturbance. This estimate is used both for feedforward compensation in the virtual controller and for online scheduling of the observer and controller bandwidths. The virtual command is finally converted through the inverse-flatness mapping into the boom-driving torque and cable-driving force. Consequently, trajectory planning, derivative reconstruction, disturbance compensation, bandwidth adaptation, and physical-input synthesis are integrated within a single closed loop.

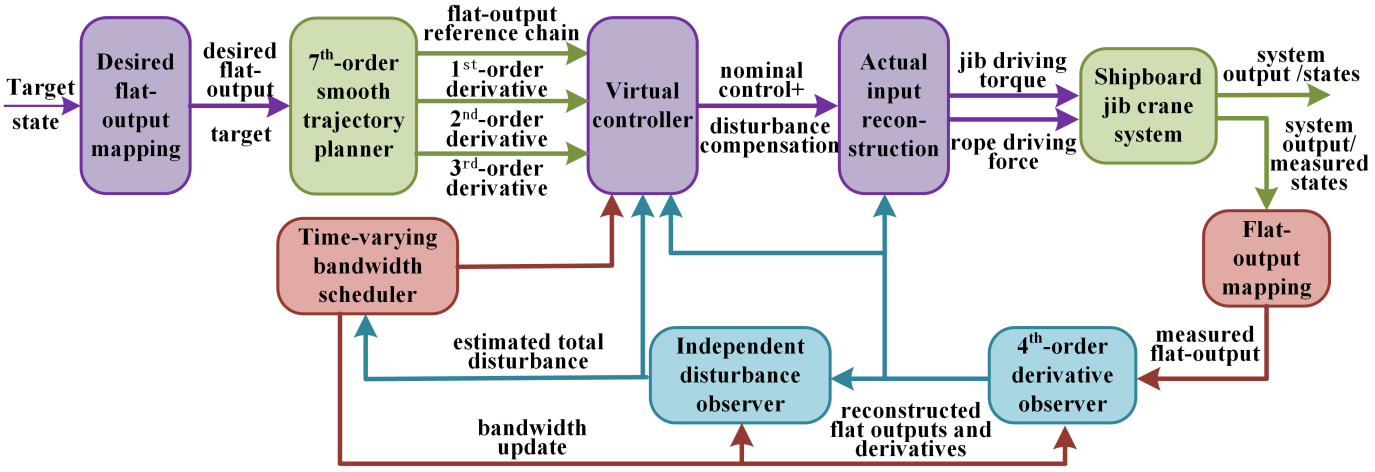


Figure 2. Overall control framework of the proposed TVB-ADRC.

First, the virtual control-input vector is introduced:

$$\boldsymbol{\nu} = \begin{bmatrix} \nu_x \\ \nu_z \end{bmatrix}, \qquad \begin{bmatrix} x_p^{(4)} \\ z_p^{(4)} \end{bmatrix} = \boldsymbol{\nu} + \mathbf{d}. \tag{25}$$

Define the state-chain vector:

$$\boldsymbol{\Gamma}_1 = \begin{bmatrix} x_p \\ z_p \end{bmatrix}, \qquad \boldsymbol{\Gamma}_i = \boldsymbol{\Gamma}_1^{(i-1)}, \quad i = 2,3,4. \tag{26}$$

Then, the flat-output channels can be uniformly written as fourth-order integrator chains:

$$\dot{\boldsymbol{\Gamma}}_1 = \boldsymbol{\Gamma}_2, \qquad \dot{\boldsymbol{\Gamma}}_2 = \boldsymbol{\Gamma}_3, \qquad \dot{\boldsymbol{\Gamma}}_3 = \boldsymbol{\Gamma}_4, \qquad \dot{\boldsymbol{\Gamma}}_4 = \boldsymbol{\nu} + \mathbf{d}. \tag{27}$$

where $\mathbf{d} \in \mathbb{R}^2$ denotes the total disturbance in the flat-output channels, encompassing modeling errors, external disturbances, and uncompensated terms.

To prevent abrupt changes in high-order reference signals from degrading the closed-loop response or driving the planned trajectory into an unfavorable operating region, a seventh-order smooth time-scaling function is used to generate the flat-output reference trajectories. Let

$$\mathbf{v}_d = \begin{bmatrix} x_{pd} \\ z_{pd} \end{bmatrix}, \qquad \mathbf{v}_0 = \begin{bmatrix} x_p(0) \\ z_p(0) \end{bmatrix}. \tag{28}$$

Then, the flat-output reference trajectories are defined as follows:

$$\mathbf{v}_1(t) = \mathbf{v}_0 + \sigma(\chi)(\mathbf{v}_d - \mathbf{v}_0), \qquad \chi = \frac{t}{T_{\text{plan}}}. \tag{29}$$

where T_{plan} denotes the reference trajectory planning duration. The seventh-order time-scaling function is selected as follows:

$$\sigma(\chi) = 35\chi^4 - 84\chi^5 + 70\chi^6 - 20\chi^7, \qquad 0 \le \chi \le 1. \tag{30}$$

Consequently, the reference signal chain for controller use can be uniformly written as follows:

$$\mathbf{v}_i(t) = \mathbf{v}_1^{(i-1)}(t), \qquad i = 2,3,4. \tag{31}$$

When $t \ge T_{\text{plan}}$, we have the following:

$$\mathbf{v}_1 = \mathbf{v}_d, \qquad \mathbf{v}_2 = 0, \qquad \mathbf{v}_3 = 0, \qquad \mathbf{v}_4 = 0. \tag{32}$$

To achieve online reconstruction of the flat-output state chain and its total disturbance, a dual-observer structure is introduced. The fourth-order derivative observer state vector is defined as follows:

$$\begin{aligned} \widehat{\mathbf{X}} &= \begin{bmatrix} \hat{\boldsymbol{\Gamma}}_1^T & \hat{\boldsymbol{\Gamma}}_2^T & \hat{\boldsymbol{\Gamma}}_3^T & \hat{\boldsymbol{\Gamma}}_4^T \end{bmatrix}^T \in \mathbb{R}^8, \\ \hat{\boldsymbol{\Gamma}}_i &= \begin{bmatrix} \hat{x}_p^{(i-1)} \\ \hat{z}_p^{(i-1)} \end{bmatrix}, \qquad i = 1,2,3,4. \end{aligned} \tag{33}$$

Meanwhile, the separate disturbance observer output and the measured flat-output residual are defined as follows:

$$\hat{\mathbf{d}} = \begin{bmatrix} \hat{d}_x \\ \hat{d}_z \end{bmatrix}, \qquad \mathbf{e} = \hat{\boldsymbol{\Gamma}}_1 - \mathbf{y}, \qquad \mathbf{y} = \begin{bmatrix} x_p \\ z_p \end{bmatrix}. \tag{34}$$

Then, the fourth-order derivative observer can be uniformly written as follows:

$$\dot{\widehat{\mathbf{X}}} = \mathbf{H}\widehat{\mathbf{X}} + \mathbf{N}(\boldsymbol{\nu} + \hat{\mathbf{d}}) - \mathbf{L}\mathbf{e}, \tag{35}$$

where

$$\begin{aligned} \mathbf{H} &= \begin{bmatrix} 0 & I & 0 & 0 \\ 0 & 0 & I & 0 \\ 0 & 0 & 0 & I \\ 0 & 0 & 0 & 0 \end{bmatrix}, \qquad \mathbf{N} = \begin{bmatrix} 0 \\ 0 \\ 0 \\ I \end{bmatrix}, \qquad \mathbf{L} = \begin{bmatrix} A_1 \\ A_2 \\ A_3 \\ A_4 \end{bmatrix}, \\ A_j &= \operatorname{diag}\{\alpha_{jx}, \alpha_{jz}\}, \qquad j = 1,2,3,4. \end{aligned} \tag{36}$$

where I denotes the 2×2 identity matrix. Further, the reference error chain is introduced:

$$\mathbf{E} = \begin{bmatrix} \mathbf{e}_1 \\ \mathbf{e}_2 \\ \mathbf{e}_3 \\ \mathbf{e}_4 \end{bmatrix} = \begin{bmatrix} \mathbf{v}_1 - \hat{\mathbf{\Gamma}}_1 \\ \mathbf{v}_2 - \hat{\mathbf{\Gamma}}_2 \\ \mathbf{v}_3 - \hat{\mathbf{\Gamma}}_3 \\ \mathbf{v}_4 - \hat{\mathbf{\Gamma}}_4 \end{bmatrix}. \tag{37}$$

The separate disturbance estimate is represented by the two observer states associated with the flat-output channels. In accordance with the implemented controller, it is generated by a residual-driven first-order leakage observer:

$$\hat{\mathbf{d}} = \begin{bmatrix} p_{51} & p_{52} \end{bmatrix}^T, \qquad \dot{\hat{\mathbf{d}}} = -\mathbf{\Lambda}_d \hat{\mathbf{d}} - \mathbf{D}_d \mathbf{e}. \tag{38}$$

The leakage and residual-injection gains are tied to the effective derivative-observer bandwidths as

$$\begin{aligned} \mathbf{\Lambda}_d &= \mathrm{diag}\{\lambda_{d,x}, \lambda_{d,z}\} = \mathrm{diag}\{\omega_{o,x}^{\mathrm{eff}}, \omega_{o,z}^{\mathrm{eff}}\}, \\ \mathbf{D}_d &= \mathrm{diag}\{d_{d,x}, d_{d,z}\} = \mathrm{diag}\{(\omega_{o,x}^{\mathrm{eff}})^5, (\omega_{o,z}^{\mathrm{eff}})^5\}. \end{aligned} \tag{39}$$

The disturbance observer is "independent" only in the sense of a separate estimate state; it shares the measured-output residual with the derivative observer. It is not an additional independent sensor, nor is unbiased disturbance reconstruction guaranteed. For a fixed observer bandwidth $\omega > 0$, the joint derivative/leakage estimation-error polynomial for one ideal channel is $(s + \omega)^5 + \omega^5$. Its roots have real parts $\omega[\cos((2j + 1)\pi/5) - 1] < 0$, $j = 0, \ldots, 4$. For a constant channel disturbance d_k, the equilibrium is $\hat{d}_k = d_k/2$, leaving $d_k/2$ uncompensated. Thus, a near-zero estimate alone cannot establish a near-zero true disturbance or compensation residual.

To balance rapid estimation and control response against noise amplification, the disturbance-estimation-driven scheduling variables are defined by

$$\rho_{o,k} = \frac{|\hat{d}_k|}{|\hat{d}_k| + s_{o,k} + \varepsilon_s}, \qquad \rho_{c,k} = \frac{|\hat{d}_k|}{|\hat{d}_k| + s_{c,k} + \varepsilon_s}, \qquad k \in \{x, z\}. \tag{40}$$

Here, $s_{o,k} > 0$ and $s_{c,k} > 0$ are disturbance-amplitude scales for observer and controller scheduling. Because the flat outputs have length units, $\hat{d}_k$, both scales, and ε_s have units $\mathrm{m/s^4}$; $\rho_{o,k}$ and $\rho_{c,k}$ are dimensionless. The implementation uses $\varepsilon_s = 10^{-12}\ \mathrm{m/s^4}$ to regularize the denominators, not as a tuning gain. The scales and bandwidth limits are listed in Table 1; all bandwidths are in $\mathrm{s^{-1}}$, and the update time constants are in seconds. The desired observer and controller bandwidths are

$$\omega_{o,k}^{\mathrm{des}} = \omega_{o,k}^{\min} + (\omega_{o,k}^{\max} - \omega_{o,k}^{\min})\rho_{o,k}, \qquad \omega_{c,k}^{\mathrm{des}} = \omega_{c,k}^{\min} + (\omega_{c,k}^{\max} - \omega_{c,k}^{\min})\rho_{c,k}. \tag{41}$$

Table 1. Controller parameter settings.

Controller	Control Gains
TVB-ADRC	$T_{\mathrm{plan}} = 4,\ T_o = 8,\ T_c = 8,\ s_{o,x} = 0.7,\ s_{o,z} = 0.7,$ $\omega_{o,x}^{\min} = 20,\ \omega_{o,x}^{\max} = 30,\ \omega_{o,z}^{\min} = 6,\ \omega_{o,z}^{\max} = 10,$ $\omega_{c,x}^{\min} = 5,\ \omega_{c,x}^{\max} = 15,\ \omega_{c,z}^{\min} = 10,\ \omega_{c,z}^{\max} = 30,$ $s_{c,x} = 5,\ s_{c,z} = 5,\ k_{p1} = 0.5,\ k_{d1} = 1,\ k_{p2} = 0.5,\ k_{d2} = 1$
ADRC	$\omega_o = 7.2,\ \overline{\omega}_o = 5.9,\ \omega_c = 2,\ \overline{\omega}_c = 1.8,\ k = 4$
ASC	$k_{\alpha l1} = 21,\ k_{\beta l1} = 6,\ k_{\alpha l2} = 14,\ k_{\beta l2} = 12,\ k_{\gamma l1} = 5,\ k_{\delta l1} = 5,$ $\gamma_1 = 1.1,\ \gamma_2 = 2,\ k_{\eta l1} = 5,\ k_{\eta l2} = 10,\ \lambda = 0.1$

Their first-order smooth update laws are

$$\dot{\omega}_{o,k} = \frac{\omega_{o,k}^{\mathrm{des}} - \omega_{o,k}}{T_o}, \qquad \dot{\omega}_{c,k} = \frac{\omega_{c,k}^{\mathrm{des}} - \omega_{c,k}}{T_c}. \tag{42}$$

and the bandwidths used in the gains are obtained through saturation:

$$\omega_{o,k}^{\mathrm{eff}} = \mathrm{sat}(\omega_{o,k}; \omega_{o,k}^{\min}, \omega_{o,k}^{\max}), \qquad \omega_{c,k}^{\mathrm{eff}} = \mathrm{sat}(\omega_{c,k}; \omega_{c,k}^{\min}, \omega_{c,k}^{\max}). \tag{43}$$

where

$$\mathrm{sat}(\xi; \xi_{\min}, \xi_{\max}) = \begin{cases} \xi_{\max}, & \xi > \xi_{\max}, \\ \xi, & \xi_{\min} \le \xi \le \xi_{\max}, \\ \xi_{\min}, & \xi < \xi_{\min}. \end{cases} \tag{44}$$

The resulting derivative-observer and controller coefficients preserve the implemented ordering and the fourth-order pole-placement polynomials:

$$\begin{aligned} \alpha_{1k} &= 4\omega_{o,k}^{\mathrm{eff}},\ \alpha_{2k} = 6(\omega_{o,k}^{\mathrm{eff}})^2,\ \alpha_{3k} = 4(\omega_{o,k}^{\mathrm{eff}})^3,\ \alpha_{4k} = (\omega_{o,k}^{\mathrm{eff}})^4, \\ p_{o,k}(s) &= s^4 + \alpha_{1k}s^3 + \alpha_{2k}s^2 + \alpha_{3k}s + \alpha_{4k} = (s + \omega_{o,k}^{\mathrm{eff}})^4, \\ \kappa_{1k} &= (\omega_{c,k}^{\mathrm{eff}})^4,\ \kappa_{2k} = 4(\omega_{c,k}^{\mathrm{eff}})^3,\ \kappa_{3k} = 6(\omega_{c,k}^{\mathrm{eff}})^2,\ \kappa_{4k} = 4\omega_{c,k}^{\mathrm{eff}}, \\ p_{c,k}(s) &= s^4 + \kappa_{4k}s^3 + \kappa_{3k}s^2 + \kappa_{2k}s + \kappa_{1k} = (s + \omega_{c,k}^{\mathrm{eff}})^4. \end{aligned} \tag{45}$$

For $j = 1, 2, 3, 4$, define the diagonal controller-gain matrix $T_j = \mathrm{diag}\{\kappa_{jx}, \kappa_{jz}\}$ from the channel coefficients in (45). The estimated-state feedback errors and the compensated virtual control input are

$$\mathbf{e}_j = \mathbf{v}_j - \hat{\mathbf{\Gamma}}_j, \qquad j = 1, 2, 3, 4, \qquad \boldsymbol{\nu} = \sum_{j=1}^{4} T_j \mathbf{e}_j - \hat{\mathbf{d}}. \tag{46}$$

The inverse-flatness reconstruction uses the observer outputs and the compensated virtual input to recover the physical boom torque and cable force. The proportional-derivative damping injection implemented for the actuated coordinates is retained as

$$\Delta_1 = -k_{d1}\hat{\dot{\eta}}_1 - k_{p1}(\hat{\eta}_1 - \eta_{1d}), \qquad \Delta_2 = -k_{d2}\hat{\dot{\eta}}_2 - k_{p2}(\hat{\eta}_2 - \eta_{2d}). \tag{47}$$

so that the accelerations used in physical-input reconstruction are

$$\hat{\ddot{\eta}}_{1,\mathrm{use}} = \hat{\ddot{\eta}}_1 + \Delta_1, \qquad \hat{\ddot{\eta}}_{2,\mathrm{use}} = \hat{\ddot{\eta}}_2 + \Delta_2. \tag{48}$$

Substitution into the inverse dynamics yields

$$\begin{aligned} M_c = {} & (J + m_p P_L^2)\hat{\ddot{\eta}}_{1,\mathrm{use}} - m_p P_L \cos(\hat{\eta}_1 - \hat{\eta}_3)\hat{\ddot{\eta}}_{2,\mathrm{use}} \\ & - m_p P_L \hat{\eta}_2 \sin(\hat{\eta}_1 - \hat{\eta}_3)\hat{\ddot{\eta}}_3 - 2m_p P_L \hat{\dot{\eta}}_2 \hat{\dot{\eta}}_3 \sin(\hat{\eta}_1 - \hat{\eta}_3) \\ & + m_p P_L \hat{\eta}_2 \cos(\hat{\eta}_1 - \hat{\eta}_3)(\hat{\dot{\eta}}_3)^2 + (m_p P_L + m_d) g \cos\hat{\eta}_1. \end{aligned} \tag{49}$$

$$\begin{aligned} F_l = {} & m_p \hat{\ddot{\eta}}_{2,\mathrm{use}} - m_p P_L \cos(\hat{\eta}_1 - \hat{\eta}_3)\hat{\ddot{\eta}}_{1,\mathrm{use}} \\ & + m_p P_L \sin(\hat{\eta}_1 - \hat{\eta}_3)(\hat{\dot{\eta}}_1)^2 - m_p \hat{\eta}_2 (\hat{\dot{\eta}}_3)^2 - m_p g \cos\hat{\eta}_3. \end{aligned} \tag{50}$$

The PD injection is part of the reported TVB-ADRC implementation. It changes the physical-input reconstruction and generally changes the actual flat-output dynamics. It is not present in the fixed-bandwidth comparator in the same form. Consequently, the recorded comparison combines scheduling, observer/controller tuning, reference generation, and PD differences; it is not a controlled isolation of scheduling alone.

3.3. Stability Analysis

The analysis below concerns the ideal virtual-input error model (27) with the observer and virtual feedback given above. It requires exact nominal inversion, or an aggregate residual that already accounts for inversion and PD-induced discrepancies and satisfies the stated input conditions. No proof is supplied that these conditions hold for the complete implemented nonlinear PD-augmented loop. In particular, equilibrium-preserving PD feedback is not, by itself, a stability proof.

Assumption 1. *The lumped disturbance and its estimate remain bounded during operation. Moreover, the residual disturbance after active compensation is bounded and asymptotically vanishing during the regulation stage; namely, there exists a constant $\bar{d}_r > 0$ such that*

$$\tilde{\mathbf{d}}(t) = \mathbf{d}(t) - \hat{\mathbf{d}}(t), \qquad \|\tilde{\mathbf{d}}(t)\| \le \bar{d}_r, \qquad \lim_{t\to\infty} \tilde{\mathbf{d}}(t) = 0. \tag{51}$$

This is a sufficient condition for the asymptotic convergence result established below. It characterizes the residual input after active disturbance compensation rather than claiming an independent unbiased-convergence property of the leakage disturbance observer. Persistent random-wave inputs need not satisfy this condition; finite-duration response records do not establish it.

Assumption 2. *The system operates in the admissible domain in which the inverse differential-flatness mapping established in Section 3.1 is continuous and nonsingular. Bounded flat outputs and required derivatives imply bounded original states, while convergence of those flat-output variables implies convergence of the original states to their corresponding limits.*

Lemma 1. *The effective observer and controller bandwidths generated by the scheduling laws are bounded. If their update rates are sufficiently small, the corresponding homogeneous derivative-observer and flat-output controller error systems are uniformly exponentially stable.*

Proof. Equations (41)–(44) give, for each flat-output channel,

$$0 < \omega_{o,k}^{\min} \le \omega_{o,k}^{\mathrm{eff}}(t) \le \omega_{o,k}^{\max}, \qquad 0 < \omega_{c,k}^{\min} \le \omega_{c,k}^{\mathrm{eff}}(t) \le \omega_{c,k}^{\max}, \qquad k \in \{x, z\}. \tag{52}$$

The desired values lie inside their specified intervals. Even if a raw initial state is outside an interval, saturation holds the effective value at its boundary until the raw state re-enters. Where the effective value varies, the raw state is inside the interval. Thus, the update law yields the almost-everywhere bounds

$$\left|\dot{\omega}_{o,k}^{\mathrm{eff}}(t)\right| \le \frac{\omega_{o,k}^{\max} - \omega_{o,k}^{\min}}{T_o}, \qquad \left|\dot{\omega}_{c,k}^{\mathrm{eff}}(t)\right| \le \frac{\omega_{c,k}^{\max} - \omega_{c,k}^{\min}}{T_c}. \tag{53}$$

The frozen observer and controller matrices associated with the coefficients in (45) have the polynomials shown there and are Hurwitz for every admissible positive bandwidth. For each frozen bandwidth, let the positive-definite Lyapunov matrix satisfy

$$A_*^T(\omega_*)P_*(\omega_*) + P_*(\omega_*)A_*(\omega_*) = -Q_*, \; Q_* > 0, \; * \in \{o, c\}. \tag{54}$$

Continuity on the compact admissible bandwidth intervals yields uniform constants such that

$$\underline{p}_* \|\xi_*\|^2 \le \xi_*^T P_*(\omega_*)\xi_* \le \overline{p}_* \|\xi_*\|^2. \tag{55}$$

Choose the parameter-dependent Lyapunov function

$$V_* = \xi_*^T P_*(\omega_*(t))\xi_*. \tag{56}$$

Its derivative is

$$\dot{V}_* = -\xi_*^T Q_* \xi_* + \xi_*^T \dot{P}_* \xi_*. \tag{57}$$

The time variation of the Lyapunov matrix is retained explicitly. Continuous differentiability on each compact bandwidth interval gives the first inequality below. Selecting sufficiently large bandwidth time constants makes the second strict inequality hold:

$$\|\dot{P}_*\| \le c_{P,*}|\dot{\omega}_*|, \qquad \|\dot{P}_*\| < \lambda_{\min}(Q_*). \tag{58}$$

Consequently,

$$\dot{V}_* \le -\left[\lambda_{\min}(Q_*) - \|\dot{P}_*\|\right]\|\xi_*\|^2 = -c_*\|\xi_*\|^2, \qquad c_* > 0. \tag{59}$$

The homogeneous time-varying observer and controller error systems are therefore uniformly exponentially stable. Hence, there exist positive constants, independent of the initial time, such that their state-transition matrices satisfy

$$\|\Phi_*(t,s)\| \le K_* e^{-\alpha_*(t-s)}, \qquad t \ge s, \quad * \in \{o,c\}. \tag{60}$$

This proves the conditional slow-variation statement. The selected time constants are not asserted to satisfy this Lyapunov sufficient inequality numerically; that certification is distinct from observed smooth traces. □

Lemma 2. *Under Assumption 1 and the slow-variation condition of Lemma 1, the fourth-order derivative-observer estimation error converges asymptotically to zero.*

Proof. Define the true flat-output chain and the estimation errors by

$$\begin{gathered} \mathbf{X} = \begin{bmatrix} \boldsymbol{\Gamma}_1^T & \boldsymbol{\Gamma}_2^T & \boldsymbol{\Gamma}_3^T & \boldsymbol{\Gamma}_4^T \end{bmatrix}^T, \qquad \widetilde{\mathbf{X}} = \mathbf{X} - \widehat{\mathbf{X}}, \\ \widetilde{\mathbf{d}} = \mathbf{d} - \hat{\mathbf{d}}, \qquad \mathbf{C} = \begin{bmatrix} I & 0 & 0 & 0 \end{bmatrix}. \end{gathered} \tag{61}$$

The measured-output residual used by the derivative and disturbance observers is

$$\mathbf{e} = \hat{\boldsymbol{\Gamma}}_1 - \mathbf{y} = \hat{\boldsymbol{\Gamma}}_1 - \boldsymbol{\Gamma}_1 = -\mathbf{C}\widetilde{\mathbf{X}}. \tag{62}$$

Subtracting the implemented derivative-observer Equation (35) from the true chain dynamics (27) gives

$$\dot{\widetilde{\mathbf{X}}} = (\mathbf{H} - \mathbf{LC})\widetilde{\mathbf{X}} + \mathbf{N}\widetilde{\mathbf{d}}, \qquad \mathbf{A}_o(t) = \mathbf{H} - \mathbf{L}(t)\mathbf{C}. \tag{63}$$

Variation of constants yields

$$\widetilde{\mathbf{X}}(t) = \Phi_o(t,0)\widetilde{\mathbf{X}}(0) + \int_0^t \Phi_o(t,s)\mathbf{N}\widetilde{\mathbf{d}}(s)\,ds. \tag{64}$$

Using the observer state-transition bound in (60),

$$\|\widetilde{\mathbf{X}}(t)\| \le K_o e^{-\alpha_o t}\|\widetilde{\mathbf{X}}(0)\| + K_o \int_0^t e^{-\alpha_o(t-s)}\|\mathbf{N}\|\,\|\widetilde{\mathbf{d}}(s)\|\,ds. \tag{65}$$

To prove that the convolution vanishes, fix any positive tolerance. Assumption 1 provides a finite time after which the residual norm is below it. Split the integral into early and tail intervals:

$$\begin{aligned} &\forall \varepsilon_d > 0,\ \exists t_0 > 0 :\ t \ge t_0 \Rightarrow \|\widetilde{\mathbf{d}}(t)\| < \varepsilon_d, \\ &I_o(t) = \int_0^t \Phi_o(t,s)\mathbf{N}\widetilde{\mathbf{d}}(s)\,ds = I_{o,1}(t) + I_{o,2}(t), \\ &I_{o,1} = \int_0^{t_0} \Phi_o(t,s)\mathbf{N}\widetilde{\mathbf{d}}(s)\,ds, \qquad I_{o,2} = \int_{t_0}^t \Phi_o(t,s)\mathbf{N}\widetilde{\mathbf{d}}(s)\,ds. \end{aligned} \tag{66}$$

Boundedness of the residual on the fixed early interval gives

$$\|I_{o,1}(t)\| \le K_o\|\mathbf{N}\|e^{-\alpha_o t}\int_0^{t_0} e^{\alpha_o s}\|\widetilde{\mathbf{d}}(s)\|\,ds \le C_o e^{-\alpha_o t} \to 0. \tag{67}$$

On the tail interval,

$$\|I_{o,2}(t)\| \le \frac{K_o\|\mathbf{N}\|}{\alpha_o}\varepsilon_d. \tag{68}$$

Because the tolerance is arbitrary, the tail bound can be made arbitrarily small, while the early-interval term and the homogeneous response decay exponentially. Therefore,

$$\lim_{t\to\infty} \widetilde{\mathbf{X}}(t) = 0. \tag{69}$$

This proves Lemma 2 under Assumption 1. □

Theorem 1. *Under Assumptions 1 and 2, provided that the observer and controller bandwidths satisfy the bounded slow-variation condition in Lemma 1, the derivative-observer estimation error and the flat-output tracking error asymptotically converge to zero.*

Proof. Define the true flat-output tracking errors and their stacked vector by

$$\boldsymbol{\varepsilon}_j = \mathbf{v}_j - \boldsymbol{\Gamma}_j, \qquad j = 1,2,3,4, \qquad \boldsymbol{\varepsilon} = \begin{bmatrix} \boldsymbol{\varepsilon}_1^T & \boldsymbol{\varepsilon}_2^T & \boldsymbol{\varepsilon}_3^T & \boldsymbol{\varepsilon}_4^T \end{bmatrix}^T. \tag{70}$$

Since $\mathbf{e}_j = \boldsymbol{\varepsilon}_j + \tilde{\boldsymbol{\Gamma}}_j$, substitution of the compensated virtual control into the true plant gives the following componentwise and stacked tracking-error dynamics:

$$\begin{aligned} &\dot{\boldsymbol{\varepsilon}}_1 = \boldsymbol{\varepsilon}_2, \qquad \dot{\boldsymbol{\varepsilon}}_2 = \boldsymbol{\varepsilon}_3, \qquad \dot{\boldsymbol{\varepsilon}}_3 = \boldsymbol{\varepsilon}_4, \\ &\dot{\boldsymbol{\varepsilon}}_4 = -\sum_{j=1}^{4} T_j \boldsymbol{\varepsilon}_j - \sum_{j=1}^{4} T_j \tilde{\boldsymbol{\Gamma}}_j - \tilde{\mathbf{d}} + \dot{\mathbf{v}}_4. \end{aligned} \tag{71}$$

$$\begin{aligned} &\dot{\boldsymbol{\varepsilon}} = \mathbf{A}_c(t)\boldsymbol{\varepsilon} + \mathbf{G}_c(t)\tilde{\mathbf{X}} + \mathbf{B}_d\tilde{\mathbf{d}} + \mathbf{B}_v\dot{\mathbf{v}}_4, \\ &\mathbf{G}_c = \mathbf{B}_c\begin{bmatrix} -T_1 & -T_2 & -T_3 & -T_4 \end{bmatrix}, \quad \mathbf{B}_d = -\mathbf{B}_c, \qquad \mathbf{B}_v = \mathbf{B}_c. \end{aligned} \tag{72}$$

Here, $\mathbf{A}_c(t)$ is the companion-form closed-loop matrix corresponding to (71), and $\mathbf{B}_c = [0\ 0\ 0\ I]^T$. Because the controller-gain matrices are generated from the bounded effective bandwidths in (52), $\mathbf{A}_c(t)$ is bounded. Lemma 1 therefore gives the following controller transition bound and total perturbation:

$$\begin{aligned} &\|\Phi_c(t,s)\| \le K_c e^{-\alpha_c(t-s)}, \qquad t \ge s, \\ &\mathbf{q}(t) = \mathbf{G}_c(t)\tilde{\mathbf{X}}(t) + \mathbf{B}_d\tilde{\mathbf{d}}(t) + \mathbf{B}_v\dot{\mathbf{v}}_4(t). \end{aligned} \tag{73}$$

By Lemma 2, Assumption 1, and the seventh-order reference planner, the derivative-observer error tends to zero, the compensation residual tends to zero as an assumed condition, and the fourth reference derivative is identically zero after the planning interval. Thus, the perturbation term is bounded and tends to zero. Variation of constants gives

$$\boldsymbol{\varepsilon}(t) = \Phi_c(t,0)\boldsymbol{\varepsilon}(0) + \int_0^t \Phi_c(t,s)\mathbf{q}(s)\,ds. \tag{74}$$

Fix any positive tolerance and a finite time after which the input norm is below it, and split the convolution:

$$\begin{aligned} &\forall \varepsilon_q > 0,\ \exists t_1 > 0 :\ t \ge t_1 \Rightarrow \|\mathbf{q}(t)\| < \varepsilon_q, \\ &I_c(t) = \int_0^t \Phi_c(t,s)\mathbf{q}(s)\,ds = I_{c,1}(t) + I_{c,2}(t), \\ &I_{c,1} = \int_0^{t_1} \Phi_c(t,s)\mathbf{q}(s)\,ds, \qquad I_{c,2} = \int_{t_1}^t \Phi_c(t,s)\mathbf{q}(s)\,ds. \end{aligned} \tag{75}$$

The fixed early interval satisfies

$$\|I_{c,1}(t)\| \le K_c e^{-\alpha_c t}\int_0^{t_1} e^{\alpha_c s}\|\mathbf{q}(s)\|\,ds \le C_c e^{-\alpha_c t} \to 0. \tag{76}$$

and the tail interval satisfies

$$\|I_{c,2}(t)\| \le \frac{K_c}{\alpha_c}\varepsilon_q. \tag{77}$$

Because the tolerance is arbitrary, the complete convolution tends to zero. The homogeneous term in (74) also decays exponentially. Combining this result with Lemma 2 gives

$$\lim_{t\to\infty} \tilde{\mathbf{X}}(t) = 0, \qquad \lim_{t\to\infty} \boldsymbol{\varepsilon}(t) = 0. \tag{78}$$

This completes the virtual-error convergence argument.

The reference limits in (32) and the tracking result give

$$\boldsymbol{\Gamma}_1 \to \mathbf{v}_d, \qquad \boldsymbol{\Gamma}_2 \to 0, \qquad \boldsymbol{\Gamma}_3 \to 0, \qquad \boldsymbol{\Gamma}_4 \to 0. \tag{79}$$

Assumption 2 and the inverse-flatness relations in Section 3.1 then imply

$$\eta_1 \to \eta_{1d}, \qquad \eta_2 \to \eta_{2d}, \qquad \eta_3 \to 0, \qquad \dot{\eta}_i \to 0, \qquad i = 1, 2, 3. \tag{80}$$

Thus, the boom angle and cable length converge to their desired values, and the payload swing vanishes within the admissible nonsingular operating domain. □

Remark 1. *The theorem concerns the specified virtual-error model, not an unconditional nonlinear hardware-loop guarantee. The PD terms vanish at the intended equilibrium, which preserves that equilibrium but does not establish its attraction. With persistent nonvanishing residuals, asymptotic convergence is replaced by an input-to-state bound, provided the same uniformly exponentially stable transition estimates hold. Let* $g_c = \sup_t \|\mathbf{G}_c(t)\|$ *and* $h_o = K_o\|\mathbf{N}\|/\alpha_o$*. Variation of constants gives, for bounded residuals and a reference whose fourth derivative tends to zero,*

$$\begin{aligned} \limsup_{t\to\infty} \|\widetilde{\mathbf{X}}(t)\| &\le h_o \bar{d}_r, \\ \limsup_{t\to\infty} \|\boldsymbol{\varepsilon}(t)\| &\le \frac{K_c}{\alpha_c}(g_c h_o + \|\mathbf{B}_d\|)\bar{d}_r. \end{aligned} \tag{81}$$

Here, $\bar{d}_r$ *may be any uniform bound on the compensation residual; its vanishing limit is not required for this bound. This is an analytic conditional bound, not a measured robustness certificate for waves, noise, or delay.*

Remark 2. *For fixed positive bandwidths, the ideal observer and controller characteristic factors are stable without a general requirement* $\omega_{o,z} > \omega_{c,z}$*. This explains why the tabulated vertical settings are not algebraically inconsistent. It does not make a slow observer preferable: the vertical derivative estimates can lag, and the leakage observer is biased under constant disturbances. These settings are empirical choices for the recorded configurations, not an optimized or universally noise-robust bandwidth separation rule. Saturation of a bandwidth limits its gain; it does not saturate actuator torque/force or guarantee exact rejection of larger disturbances.*

4. Simulation and Experimental Results

4.1. Simulation Setup and Performance Indices

The archived MATLAB/Simulink responses compare TVB-ADRC with fixed-bandwidth ADRC [19] and ASC [18]. No new simulation is claimed in this reanalysis. The five logged groups are boom angle (degrees), cable length (m), swing angle (degrees), boom torque (N m), and cable generalized force (N). The first three columns follow the TVB-ADRC, ADRC, and ASC branch order; the fourth contains the reference or static compensation level. This order is supported by the archived root Mux connections and plotting scripts. Older source legends MASC and EBC (or ADRC) correspond to TVB-ADRC and ADRC in the text. Static model inspection is supporting provenance, not proof that the saved model exactly reproduces every historical run. The nominal simulation parameters are

$$\begin{aligned} &m_p = 2.0\,\text{kg}, \quad P_L = 0.7\,\text{m}, \quad m_d = 5.49\,\text{kg m}, \\ &g = 9.8\,\text{m/s}^2, \quad J = 6.5\,\text{kg}\cdot\text{m}^2, \quad c_\theta = 0.05\,\text{N m s/rad}. \end{aligned}$$

Except for the modified conditions specified in Cases 4–6, the initial and target transformed states shown in the response plots are

$$\begin{aligned} &\eta_1(0) = 10^\circ, \quad \eta_2(0) = 0.10\,\text{m}, \quad \eta_3(0) = 0^\circ, \\ &\eta_{1d} = 55^\circ, \quad \eta_{2d} = 0.35\,\text{m}, \quad \eta_{3d} = 0^\circ. \end{aligned}$$

The reported configurations are listed in Table 1; they are retained rather than retuned retrospectively to improve rankings. In the archived initialization script, $m_b = 18\,\text{kg}$

and $d_b = 0.305\,\mathrm{m}$, so $m_d = 5.49\,\mathrm{kg\,m}$. The nominal target gravity-compensation torque is $(m_p P_L + m_d)g\cos 55^\circ = 38.7290\,\mathrm{N\,m}$, matching the logged fourth torque column; this resolves the earlier approximately 11 versus 40 N m inconsistency. Simulation and laboratory inertia values concern different configurations and are not interchanged. For ADRC, unbarred/barred bandwidths denote x/z; the ASC gains are method-specific. The table's γ_1, γ_2 are ASC coefficients, not bandwidth update times.

The author-designated common MSS configuration is the ITTC spectrum, $H_s = 0.1\,\mathrm{m}$, modal angular frequency 2 rad/s, mean direction 0 rad, spreading parameter 1, infinite depth, 20 frequency components, 10 directions, energy parameter 0.005, frequency cutoff 3, direction cutoff 0, seed 123, and randomized frequencies/directions enabled. These are the recorded GUI settings, not an identified vessel response. Figure 3 is a sea-surface illustration, not roll/heave validation. The archived MSS wave-velocity output connects to a separate generalized-disturbance port in the plant; a calibrated conversion to vessel roll/heave or generalized load is not documented. Moreover, a saved historical model has branch-specific spreading settings of 1, 1, 2 and other configuration differences. Consequently, identical historical forcing across methods and a physical vessel-response reconstruction cannot be independently certified from the available archive. The response metrics below describe the saved records and are not a claim of a newly standardized sea-state rerun.

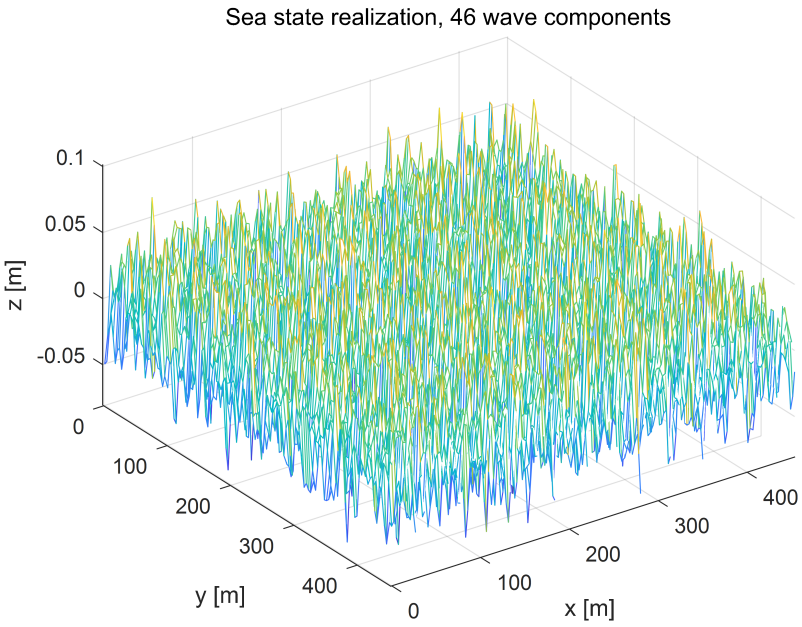


Figure 3. Archived visualization of a generated sea surface; no vessel-motion transfer model is identified from this image.

All six simulation records contain 4001 samples on $0 \le t \le 20\,\mathrm{s}$ at 0.005 s spacing. Reanalysis uses the absolute-error bands 0.8° (boom), 0.005 m (cable), and 0.5° (swing) about the logged constant targets. For each channel, t_{η_i} denotes the first sample after its last recorded out-of-band sample, or zero if the entire record is in band; a channel out of band at the last sample is not assigned a finite value. These are *finite-window last-entry times*, not guaranteed asymptotic settling times. The definition is a transparent common reanalysis convention, not a recovered original measurement protocol. The maximum swing is $\max|\eta_3|$. Case 3 uses $t \ge 10\,\mathrm{s}$ and reports last-entry time relative to 10 s, together with $\max_{t\ge 10}|M_c(t) - M_{c,\mathrm{static}}|$. Previously verified values for the reverse-positioning and nonzero-initial-swing cases are retained; at half-sample decimal ties, inherited two-decimal rounding is retained. Exact sample-level values and read-only integrity hashes accompany the reanalysis. Laboratory summary times have not been recomputed under this convention.

4.2. Nominal Performance and Disturbance Recovery

Cases 1–3 compare the controllers under disturbance-free conditions, continuous random-wave excitation, and combined wave and impulse disturbances, respectively.

4.2.1. Case 1: Disturbance-Free Operation

Under disturbance-free conditions, Figure 4 and Table 2 show that all controllers reach the desired boom angle and cable length. TVB-ADRC achieves a small peak swing (0.71°), close to ADRC (0.70°) and much lower than ASC (4.03°), while giving shorter boom-angle and cable-length last-entry times than ADRC. Its swing last-entry time is longer than those of both benchmarks. This case therefore shows faster actuated-state regulation with a peak swing close to ADRC, rather than uniformly faster swing suppression.

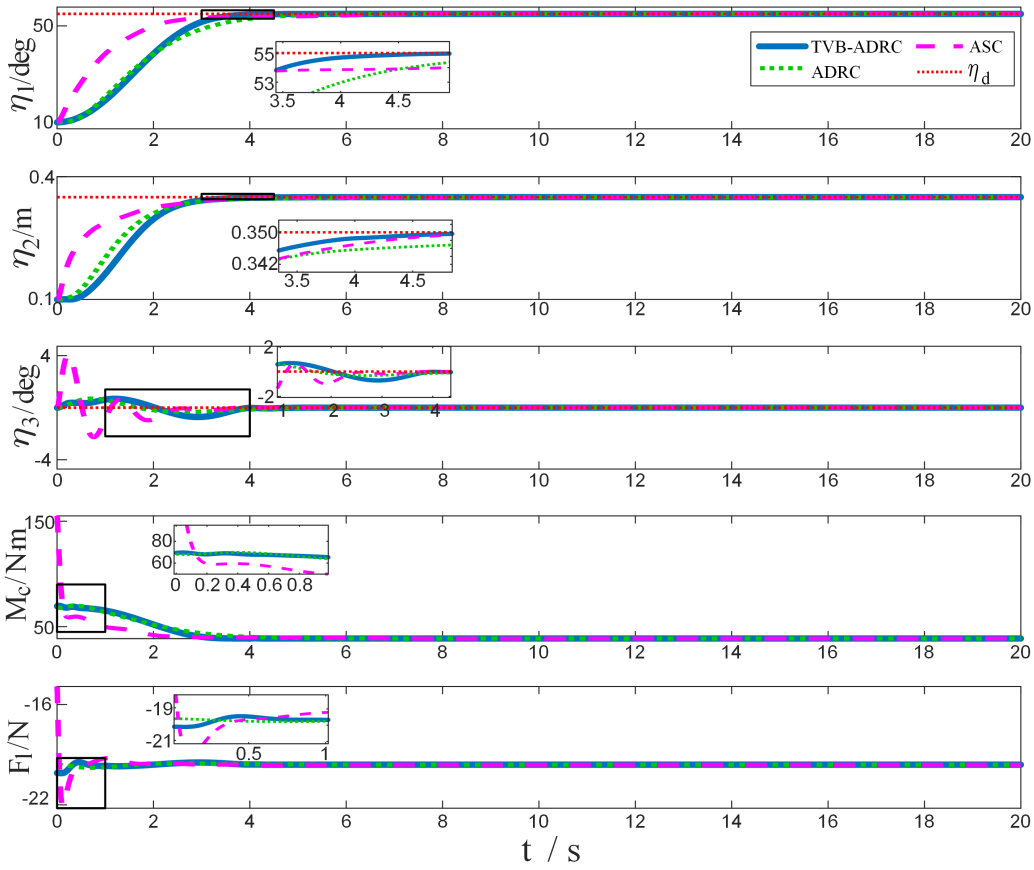


Figure 4. System responses of the three controllers under disturbance-free conditions.

Table 2. Performance comparison under disturbance-free conditions.

Method	$\eta_{3\max}$ (deg)	t_{η_3} (s)	t_{η_1} (s)	t_{η_2} (s)
TVB-ADRC	0.71	3.38	3.60	3.29
ADRC	0.70	1.13	4.77	3.73
ASC	4.03	2.21	5.56	3.60

4.2.2. Case 2: Continuous Random-Wave Disturbance

For the archived wave run, Figure 5 shows the recorded responses, while Table 3 summarizes the reproducible last-entry times. The ADRC values 19.68, 19.97, and 19.95 s leave only about 0.32, 0.035, and 0.05 s of observed in-band tail, respectively; they cannot support a claim of sustained settling in persistent waves. The final-two-second error metrics in Appendix A provide a less ambiguous finite-record comparison. TVB-ADRC has a larger

peak swing than ADRC but a smaller peak swing than ASC, whereas ASC has the shorter swing last-entry time. Thus, no uniformly best swing response is claimed.

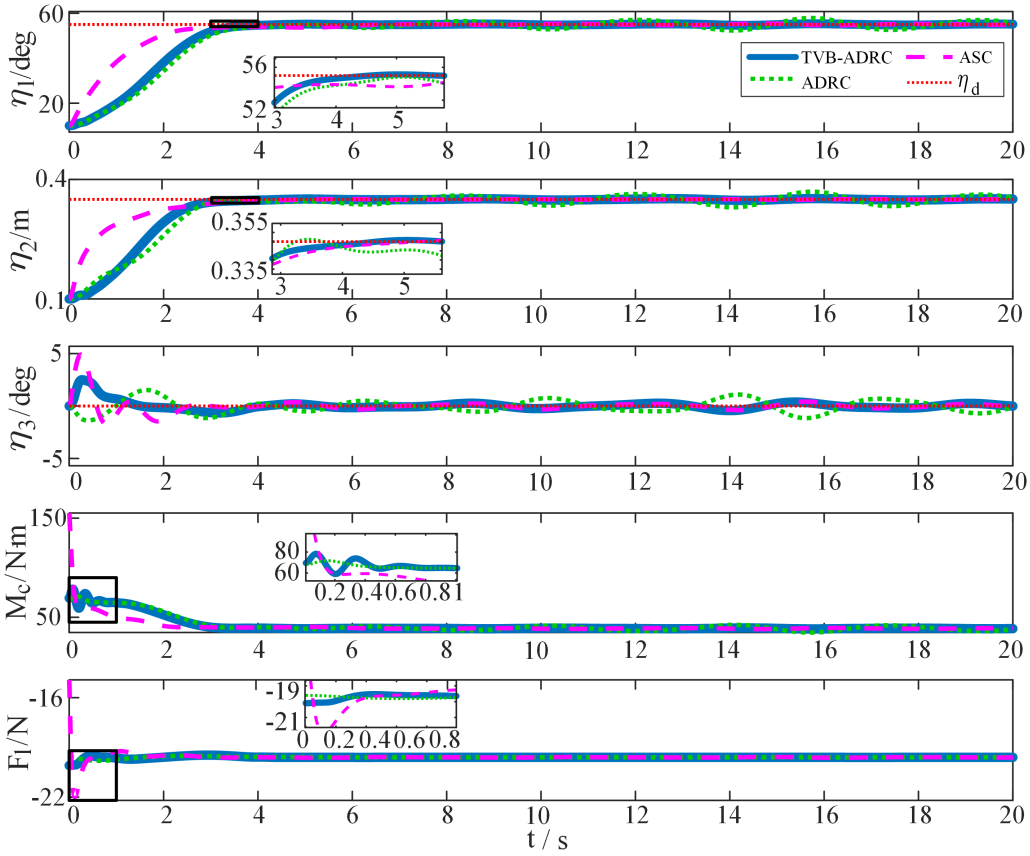


Figure 5. System responses of the three controllers under continuous random-wave disturbance.

Table 3. Performance comparison under continuous random-wave disturbance.

Method	$\eta_{3\max}$ (deg)	t_{η_3} (s)	t_{η_1} (s)	t_{η_2} (s)
TVB-ADRC	2.51	3.54	3.60	3.19
ADRC	1.52	19.68	19.97	19.95
ASC	4.90	2.31	5.83	3.57

4.2.3. Case 3: Combined Wave and Impulse Disturbances

An additional positive rectangular pulse of 4 N m is applied to the boom generalized-torque channel over $10 \le t < 11$ s, superposed on the wave excitation. The same pulse amplitude, duration, timing, and input channel are used for all three control methods. Figure 6 shows the corresponding responses, and Table 4 reports the post-10 s metrics. Relative to the stated static-torque baseline, the incremental maxima are 6.87, 20.50, and 19.50 N m. These values use the explicitly defined baseline and unchanged recorded torque samples.

Table 4. Local recovery performance under combined wave and impulse disturbances.

Method	$\eta_{3\max,\mathrm{post}}$ (deg)	$t_{\eta_3,\mathrm{rec}}$ (s)	$t_{\eta_1,\mathrm{rec}}$ (s)	$t_{\eta_2,\mathrm{rec}}$ (s)	$\Delta M_{c,\max}$ (N m)
TVB-ADRC	0.98	1.96	1.94	2.17	6.87
ADRC	1.68	9.68	9.97	9.95	20.50
ASC	1.61	5.81	7.30	3.23	19.50

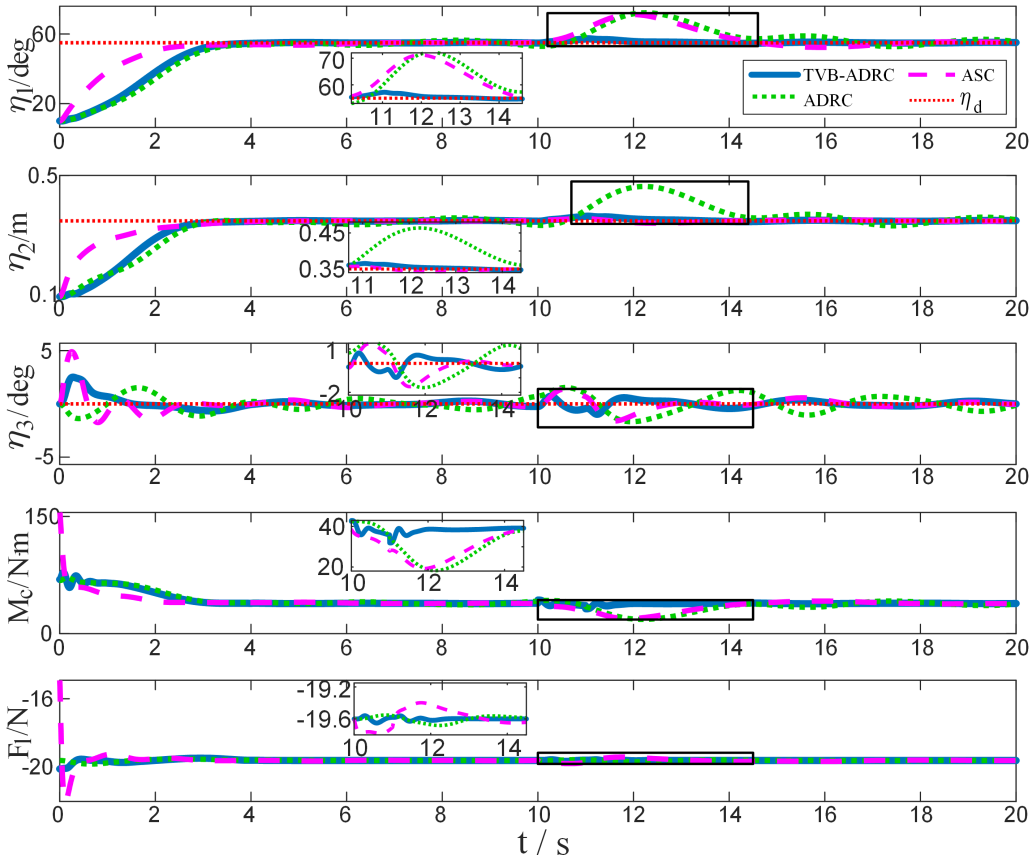


Figure 6. System responses of the three controllers under combined wave and impulse disturbances.

4.3. Adaptability to Reference, Load, and Initial-State Changes

Cases 4–6 examine reverse positioning, fixed lower-payload operation, and nonzero initial swing, respectively.

4.3.1. Case 4: Reverse Positioning

This is a separate reverse-positioning run beginning at $t = 0$, not a target switch during a previously settled run. Its initial state is $[55°, 0.55\,\text{m}, 0°]^T$, and its target is $[10°, 0.10\,\text{m}, 0°]^T$. Figure 7 and Table 5 show a similar peak swing for the two ADRC configurations, but the shortest swing last-entry time belongs to ADRC. TVB-ADRC has the shorter boom/cable last-entry times; ASC reaches a 13.50° swing peak.

Table 5. Reverse-positioning performance using finite-window last-entry times.

Method	$\eta_{3\max}$ (deg)	t_{η_3} (s)	t_{η_1} (s)	t_{η_2} (s)
TVB-ADRC	0.72	3.33	4.29	5.02
ADRC	0.72	1.11	5.92	6.27
ASC	13.50	3.67	12.54	8.17

4.3.2. Case 5: Lower-Payload Operation

This case is a separate run with a fixed lower payload of 1 kg, compared with the nominal 2 kg configuration; no within-run payload change is applied. The static force and torque references are −9.8 N and 34.7943 N m, respectively, consistent with this lower payload. The case evaluates the reported control configurations under lower-payload operation, not their robustness to an abrupt unknown mass change or an unverified compensation-mass mismatch. Figure 8 shows the recorded responses, and Table 6 reports the metrics using the

common finite-window last-entry convention. TVB-ADRC has a shorter swing last-entry time than ASC but a longer swing last-entry time than ADRC.

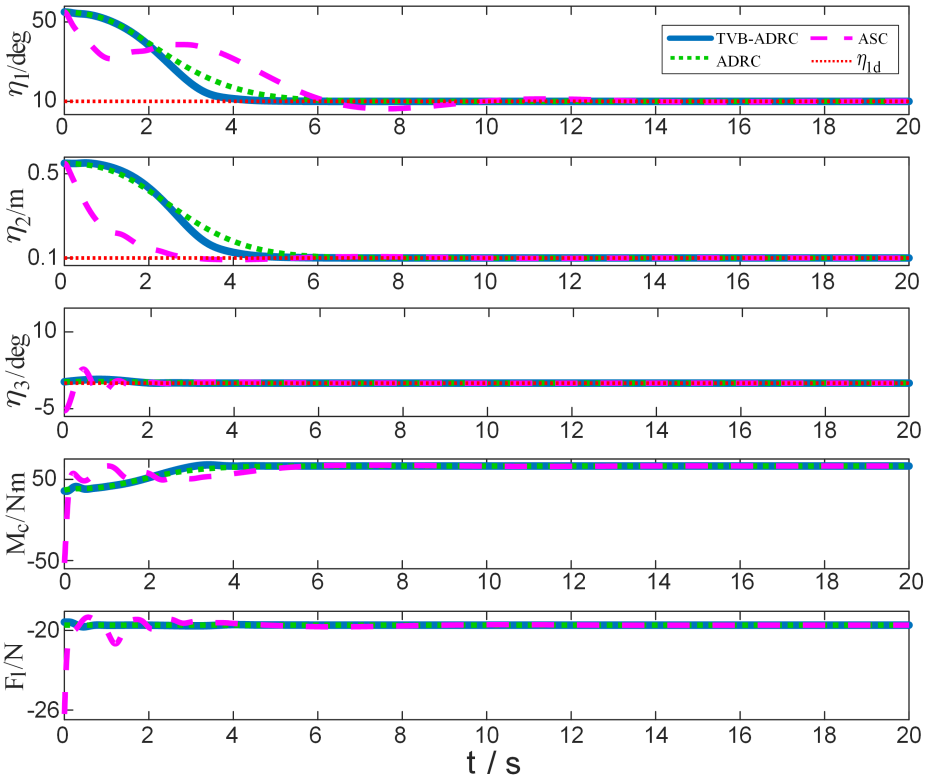


Figure 7. System responses in a separate reverse-positioning run initiated at $t = 0$.

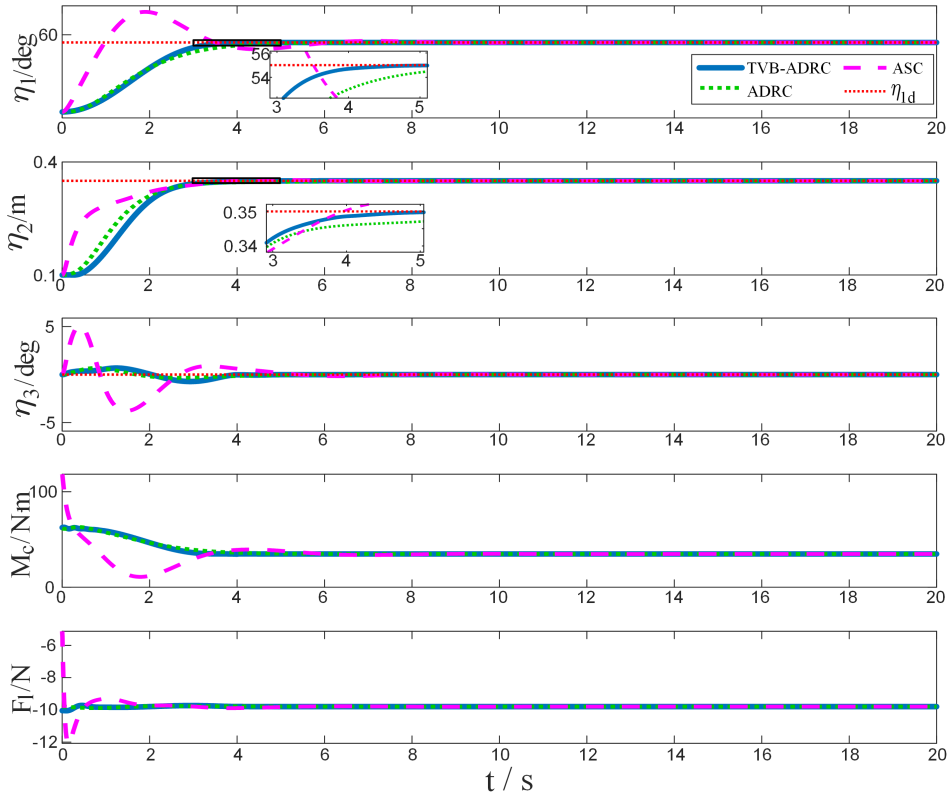


Figure 8. System responses of the three controllers for the fixed lower-payload case.

Table 6. Performance comparison for fixed lower-payload operation.

Method	$\eta_{3\max}$ (deg)	t_{η_3} (s)	t_{η_1} (s)	t_{η_2} (s)
TVB-ADRC	0.72	3.39	3.60	3.27
ADRC	0.69	1.15	4.76	3.59
ASC	5.08	4.27	7.63	3.47

4.3.3. Case 6: Nonzero Initial Swing

The initial swing is 2° for all methods; the boom/cable initial values and targets are the nominal ones. Figure 9 shows the corresponding responses, and Table 7 reports the independently verified metrics rather than copying Table 5. TVB-ADRC and ADRC do not exceed the imposed 2° initial swing, while ASC reaches 3.88°. ADRC has the shortest swing last-entry time; TVB-ADRC has the shortest boom/cable times.

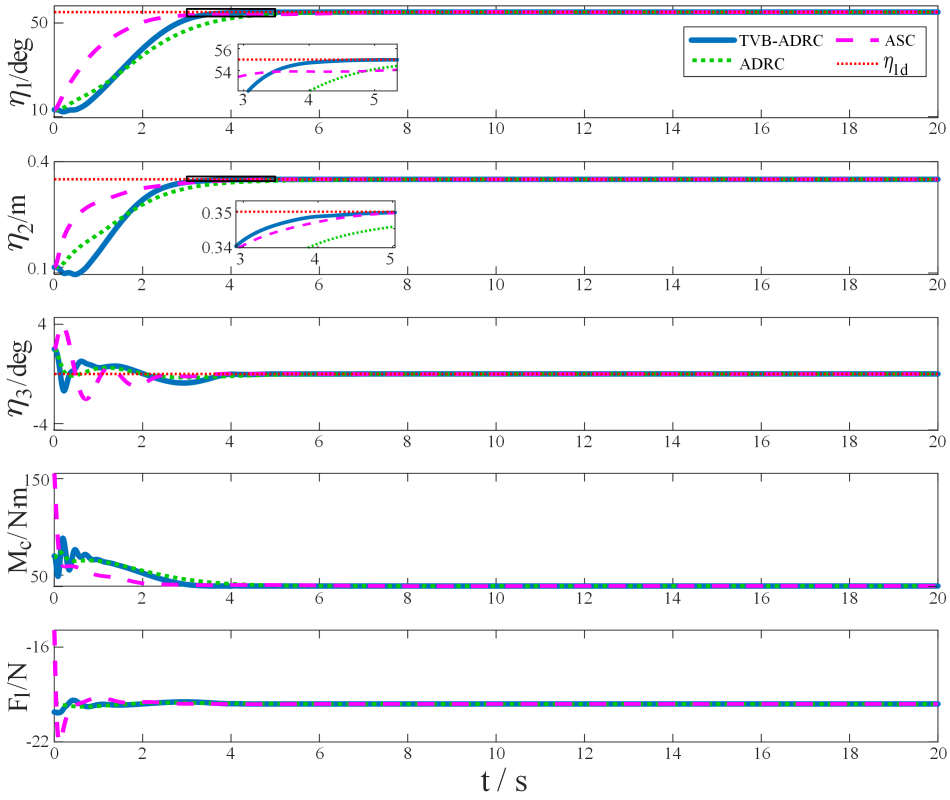


Figure 9. System responses of the three controllers with a nonzero initial swing angle.

Table 7. Recorded performance with a 2° initial swing; times use the finite-window definition.

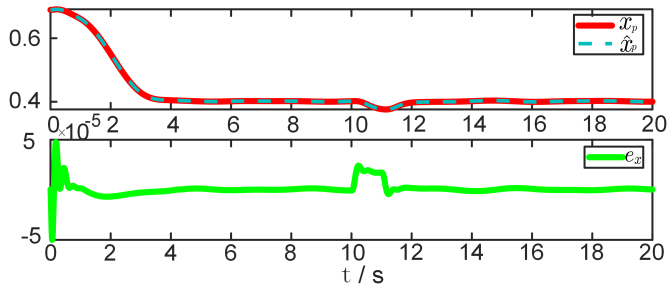
Method	$\eta_{3\max}$ (deg)	t_{η_3} (s)	t_{η_1} (s)	t_{η_2} (s)
TVB-ADRC	2.00	3.39	3.58	3.30
ADRC	2.00	1.22	5.08	4.83
ASC	3.88	2.16	5.67	3.61

4.4. Flat-Output Derivative Observation and Bandwidth-Scheduling Results

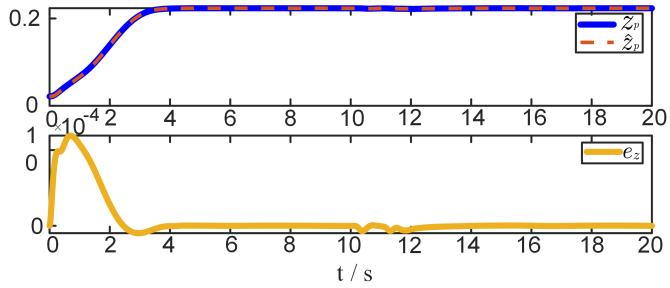
The preceding records illustrate complete-controller response differences. The following archived plots illustrate internal signals; they do not independently isolate the causal contribution of scheduling.

Figure 10 shows the estimates and errors for the two flat-output channels. After short initial transients, the plotted flat-output estimates approach the true signals, and their errors

remain small. These plots show the accuracy of the measured-output estimates; they do not directly display the errors of all higher-order derivative estimates.



(**a**)



(**b**)

Figure 10. Observation results and error curves for the two flat-output channels: (**a**) x_p channel and (**b**) z_p channel.

Figure 11 displays the leakage disturbance estimates. Their small late-time amplitude is not a measurement of the true disturbance-estimation error. In particular, the constant-disturbance bias discussed in Section 3.3 prevents interpreting a small estimate as proof of asymptotically exact compensation.

Figure 12 is retained as an archived raw-bandwidth-state plot. The saved scope wiring logs integrator states before clipping, whereas the implemented gains use the clipped effective values. The vertical-controller raw state is initialized from the vertical-observer lower bound ($6\,s^{-1}$ in the saved setup), below its controller lower bound of $10\,s^{-1}$. This explains how a trace below 10 can coexist with a gain floor of 10; it does not make that raw trace an effective gain. The original numeric trace has not been independently re-exported, so no new effective-bandwidth curve is fabricated. Small plotted excursions cannot substantiate a large scheduling benefit. A matched on/off ablation with identical PD, planner, reference, and forcing is required to quantify that benefit.

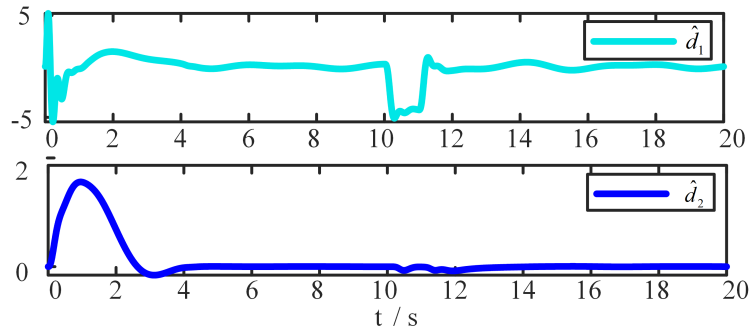


Figure 11. Leakage disturbance estimates for the two channels. The source-plot labels $\hat{d}_1$ and $\hat{d}_2$ correspond to $\hat{d}_x$ and $\hat{d}_z$, respectively.

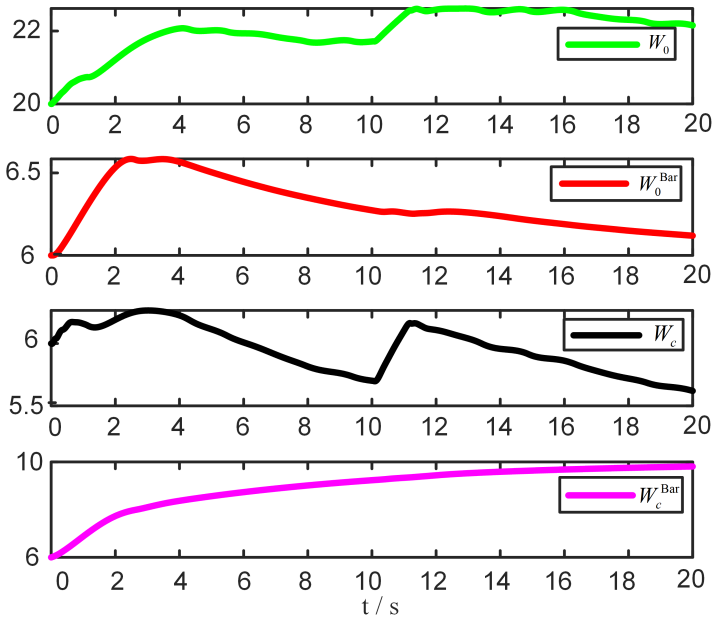


Figure 12. Archived raw bandwidth states (not clipped effective gain values). Source labels W_0, W_0^{Bar}, W_c, and W_c^{Bar} denote the x/z observer and controller states. The implemented gain bandwidths are their saturations in (43).

4.5. Hardware Experiments

The laboratory platform in Figure 13 is used to compare the three control configurations for boom positioning, cable-length regulation, and load-swing suppression. The control system is implemented in MATLAB/Simulink (R2026b) with OMRON encoders (model designation: EB-CWZX; resolution: 2500 pulses per revolution, P/R) and a sampling period of 0.005 s. The prescribed roll and heave excitation signals used in the physical experiment are

$$\varphi(t) = \frac{5\pi}{180}\sin(0.75t)\ \mathrm{rad}, \qquad h(t) = 0.05\sin(0.75t)\ \mathrm{m}, \tag{82}$$

where t is in seconds, φ denotes the roll excitation, and h denotes the heave excitation, consistent with the motion notation in the model. The amplitudes are 5° and 0.05 m, respectively, and the common angular frequency is 0.75 rad/s. These prescribed signals represent periodic wave excitation in the laboratory; they are not the stochastic MSS wave field used in the numerical simulations. Accordingly, the hardware results are not interpreted as validation under an equivalent random sea state or general multi-degree-of-freedom vessel motion.

The laboratory parameter values, including the provisional mass-moment estimate explained below, are

$$m_p = 2.0\,\mathrm{kg}, \quad P_L = 0.65\,\mathrm{m}, \quad m_d \approx 0.75\,\mathrm{kg\cdot m},$$
$$J = 0.32\,\mathrm{kg\cdot m^2}, \quad g = 9.81\,\mathrm{m/s^2}.$$

Here, m_p is the payload mass, P_L is the equivalent boom length, m_d is the boom mass-moment parameter, and J is the equivalent boom inertia. The laboratory payload mass and equivalent boom length are 2.0 kg and 0.65 m, respectively. The value $m_d \approx 0.75\,\mathrm{kg\cdot m}$ is an estimate inferred from the late-time input level for the nominal static interpretation below; it is not an independently measured mass moment or confirmation of the value used in the original controller implementation. The simulation and laboratory parameter sets are

listed separately because they describe different configurations; the simulation settings and archived recordings are unchanged. The initial and target transformed states are

$$\eta_1(0) = 0^\circ, \quad \eta_2(0) = 0.10\,\mathrm{m}, \quad \eta_3(0) = 0^\circ,$$
$$\eta_{1d} = 35^\circ, \quad \eta_{2d} = 0.35\,\mathrm{m}, \quad \eta_{3d} = 0^\circ.$$

The experimental scheduling and damping parameters are

$$T_{\mathrm{plan}} = 4,\ T_o = 8,\ T_c = 8,\ s_{o,x} = 0.35,\ s_{o,z} = 0.40,$$
$$\omega_{o,x}^{\min} = 10,\ \omega_{o,x}^{\max} = 18,\ \omega_{o,z}^{\min} = 3.5,\ \omega_{o,z}^{\max} = 6.5,\ s_{c,x} = 2.2,$$
$$\omega_{c,x}^{\min} = 2.8,\ \omega_{c,x}^{\max} = 6.5,\ \omega_{c,z}^{\min} = 4.5,\ \omega_{c,z}^{\max} = 12,\ s_{c,z} = 2.5,$$
$$k_{p1} = 0.28,\ k_{d1} = 0.85,\ k_{p2} = 0.32,\ k_{d2} = 0.85.$$

The laboratory gains are specified separately from the simulation gains. The bandwidth update time constants are $T_o = T_c = 8\,\mathrm{s}$; they are not increased relative to the corresponding simulation values.

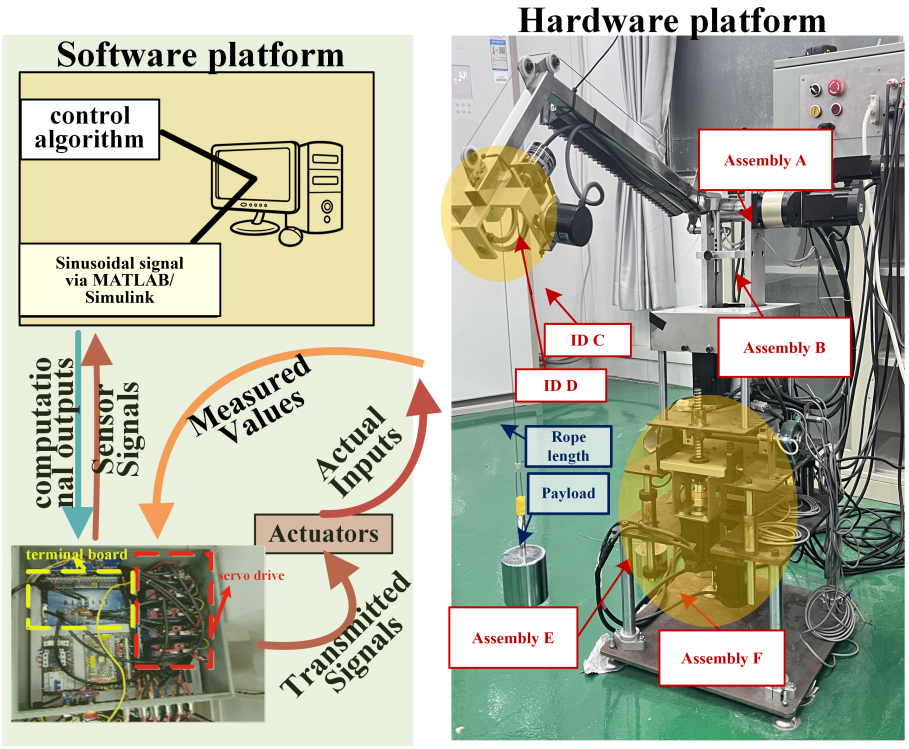


Figure 13. Laboratory crane platform and control arrangement. Labels A–F distinguish the visible assemblies and replace the duplicated motor identifiers in the original photograph; they do not assign unverified actuator or sensor channels. The software disturbance label refers to the sinusoidal physical experiment, not the stochastic MSS simulation.

Figure 14 and Table 8 compare the laboratory responses. TVB-ADRC has a reported peak swing of 2.79°, compared with 4.51° for ADRC and 6.01° for ASC, and the shortest reported swing-regulation time. The actuated-state times are not uniformly smaller, and ADRC has lower input peaks. These results compare the complete controller configurations rather than an isolated bandwidth-scheduling mechanism. No noise-injection or delay-sensitivity test is inferred from this experiment.

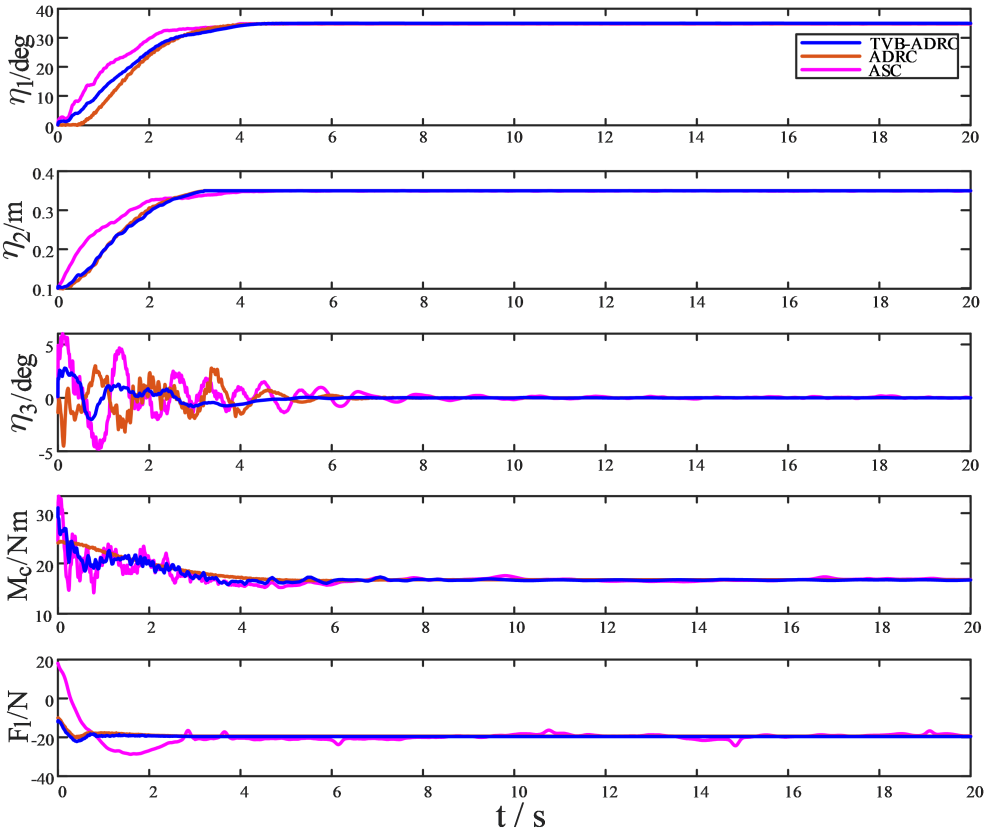


Figure 14. Laboratory responses under prescribed sinusoidal disturbance: boom angle, cable length, load swing, and control-input channels. The nominal input-level interpretation uses an inferred mass-moment estimate, as discussed in the text.

Table 8. Laboratory transient-performance comparison under prescribed sinusoidal disturbance. The mass-moment estimate used for nominal input interpretation is identified in the text.

Method	$\eta_{3\max}$ (deg)	t_{η_3} (s)	t_{η_1} (s)	t_{η_2} (s)	$M_{c,\max}$ (N m)	$F_{l,\max}$ (N)
TVB-ADRC	2.79	4.16	4.03	3.04	31.06	22.17
ADRC	4.51	4.77	3.81	2.99	24.39	20.10
ASC	6.01	6.66	3.84	3.78	33.38	28.69

For $m_p = 2.0\,\mathrm{kg}$ and $P_L = 0.65\,\mathrm{m}$, the nominal static relations at $\eta_1 = 35^\circ$ give

$$F_{l,\mathrm{eq}} = -m_p g = -19.62\,\mathrm{N}, \qquad M_{c,\mathrm{eq}} = (m_p P_L + m_d) g \cos 35^\circ \approx 16.5\,\mathrm{N\,m}$$

when $m_d \approx 0.75\,\mathrm{kg \cdot m}$. These nominal levels are consistent in magnitude with the plotted late-time force of about $-20\,\mathrm{N}$ and torque of about 16–17 N m. The negative force sign follows the generalized-input convention. Because m_d was inferred from the same response, this agreement is a static consistency check, not independent identification of the platform parameters or validation of the complete transient response and actuator-input calibration. No archived input trace is modified by this interpretation.

The prescribed sinusoidal disturbance provides a laboratory illustration of periodic-disturbance operation. The stated 2500 P/R is the encoder pulse resolution, not a measured installed-angle accuracy. The specified excitation signals do not establish the installed zeroing accuracy or a measured platform-motion tracking accuracy; no corresponding sensor-robustness or random-sea-state claim is made.

5. Conclusions

A disturbance-estimation-driven bandwidth-scheduling framework has been formulated for flatness-based control of shipboard boom cranes. The derivative observer, leakage disturbance observer, and bounded bandwidth update laws are specified separately. The analysis establishes convergence of an ideal virtual-error model under the stated residual and transition conditions, and an ultimate error bound for a bounded nonvanishing residual. It does not establish unconditional convergence of the complete nonlinear PD-augmented loop under persistent disturbance.

Across six simulation cases, the complete TVB-ADRC configuration offers faster actuated-state regulation in several comparisons, while the swing and input metrics show nonuniform trade-offs. The laboratory experiment with prescribed sinusoidal disturbance gives a reported 2.79° peak swing and illustrates positioning and swing suppression under periodic excitation. An inferred mass-moment estimate reconciles the nominal late-time input magnitudes, but this agreement is not independent validation of the physical parameters. Since the compared configurations differ in tuning and auxiliary compensation, these results do not quantify the independent benefit of bandwidth scheduling. The conclusions are confined to the reported configurations and excitation conditions, without extending them to quantified noise/delay robustness or general vessel-motion rejection.

Author Contributions: Conceptualization, Y.H. and L.C.; Methodology, L.C.; Software, L.C.; Validation, L.C.; Formal analysis, L.C.; Investigation, L.C., T.W., J.Y., C.X. and X.H.; Resources, T.W., X.W. and W.H.; Data curation, L.C.; Writing—original draft, L.C.; Writing—review & editing, Y.H.; Visualization, L.C.; Supervision, Y.H.; Project administration, Y.H. All authors have read and agreed to the published version of the manuscript.

Funding: This research was funded by the Key Field Special Project of General Higher Education Institutions in Guangdong Province (New Generation Electronic Information [Semiconductor]), grant number 2024ZDZX1009; the Natural Science Foundation of Guangxi, grant number 2025GXNSFHA069191; and the Research Capacity Enhancement Project for Key Construction Disciplines of Guangdong Province, grant number 2025ZDJS059.

Data Availability Statement: The original contributions presented in this study are included in the article. Further inquiries can be directed to the corresponding authors.

Conflicts of Interest: Xiaodong Wang is employed by Guangdong Kejie Technology Co., Ltd.; Chuanbin Xu is employed by Shenzhen Sinovo Electric Technologies Co., Ltd.; and Xiangjun He is employed by Guangdong Tiandi Intelligent Equipment Co., Ltd. The remaining authors declare that they have no conflicts of interest.

Abbreviations

The following abbreviations are used in this manuscript:

ADRC	Active disturbance rejection control
TVB-ADRC	Time-varying bandwidth active disturbance rejection control
ASC	Active swing control
MSS	Marine Systems Simulator

Appendix A. Finite-Record Error and Input Indices

For a sampled error e, $\mathrm{RMSE}_{[18,20]}(e) = \sqrt{N^{-1}\sum_{18\le t_i\le 20} e(t_i)^2}$. The input RMS values below use the entire $[0, 20]$ s record, $\sqrt{4001^{-1}\sum_i u_i^2}$, including static compensation. They are not normalized energy measures or noise-robustness tests. No sample is filtered, rescaled, or replaced. The archived wave run gives the following indices, summarized in Table A1.

Table A1. Wave-run final-two-second tracking RMSE and full-record input RMS.

Method	Boom (deg)	Cable (m)	Swing (deg)	Torque (N m)	Force (N)
TVB-ADRC	0.1539	0.001056	0.1602	42.253	19.600
ADRC	1.3549	0.008492	0.4530	42.597	19.600
ASC	0.1558	0.000331	0.1162	41.134	19.602

The final-two-second maximum absolute errors for TVB-ADRC, ADRC, and ASC are, respectively, $(0.210^\circ, 0.001413\,\text{m}, 0.254^\circ)$, $(1.960^\circ, 0.012208\,\text{m}, 0.700^\circ)$, and $(0.241^\circ, 0.000468\,\text{m}, 0.192^\circ)$, ordered as boom, cable, and swing. These values clarify the very short terminal in-band tails in Table 3 without claiming behavior beyond the recorded 20 s. The accompanying audit CSV also reports every case's raw-precision last-entry time, peak/RMS input, and discrete total variation $\sum_i |u_{i+1} - u_i|$; the latter depends on sample spacing and is not a continuous-time variation estimate.

References

1. Yang, L.; Ma, X.; Jiang, G.; Yang, H.; Yu, Y. Nonlinear control of offshore cranes for underwater payload transportation under wave-induced ship motions with full-state constraints. *Ocean Eng.* **2026**, *351*, 124471. [CrossRef]
2. Cao, Y.; Li, T.; Hao, L.-Y.; Gao, X. Nonlinear antiswing control of shipboard boom cranes using MPC-based auto-tuning mechanism with full state constraints. *IEEE Trans. Intell. Transp. Syst.* **2024**, *25*, 2281–2292. [CrossRef]
3. Lu, B.; Fang, Y.; Sun, N.; Wang, X. Antiswing control of offshore boom cranes with ship roll disturbances. *IEEE Trans. Control Syst. Technol.* **2018**, *26*, 740–747. [CrossRef]
4. Sun, N.; Fang, Y.; Chen, H.; Fu, Y.; Lu, B. Nonlinear stabilizing control for ship-mounted cranes with ship roll and heave movements: Design, analysis, and experiments. *IEEE Trans. Syst. Man Cybern. Syst.* **2018**, *48*, 1781–1793. [CrossRef]
5. Fasih ur Rehman, S.M.; Mohamed, Z.; Husain, A.R.; Jaafar, H.I.; Shaheed, M.H.; Abbasi, M.A. Input shaping with an adaptive scheme for swing control of an underactuated tower crane under payload hoisting and mass variations. *Mech. Syst. Signal Process.* **2022**, *175*, 109106. [CrossRef]
6. Li, G.; Ma, X.; Li, Z.; Li, Y. Time-polynomial-based optimal trajectory planning for double-pendulum tower crane with full-state constraints and obstacle avoidance. *IEEE/ASME Trans. Mechatron.* **2023**, *28*, 919–932. [CrossRef]
7. Vu, M.N.; Lobe, A.; Beck, F.; Weingartshofer, T.; Hartl-Nesic, C.; Kugi, A. Fast trajectory planning and control of a lab-scale 3D gantry crane for a moving target in an environment with obstacles. *Control Eng. Pract.* **2022**, *126*, 105255. [CrossRef]
8. Fu, Y.; Sun, N.; Yang, T.; Qiu, Z.; Fang, Y. Adaptive coupling anti-swing tracking control of underactuated dual boom crane systems. *IEEE Trans. Syst. Man Cybern. Syst.* **2022**, *52*, 4697–4709. [CrossRef]
9. Yang, T.; Sun, N.; Fang, Y. Adaptive fuzzy control for a class of MIMO underactuated systems with plant uncertainties and actuator deadzones: Design and experiments. *IEEE Trans. Cybern.* **2022**, *52*, 8213–8226. [CrossRef] [PubMed]
10. Yang, T.; Chen, H.; Sun, N.; Fang, Y. Adaptive neural network output feedback control of uncertain underactuated systems with actuated and unactuated state constraints. *IEEE Trans. Syst. Man Cybern. Syst.* **2022**, *52*, 7027–7043. [CrossRef]
11. Yang, T.; Sun, N.; Fang, Y. Neuroadaptive control for complicated underactuated systems with simultaneous output and velocity constraints exerted on both actuated and unactuated states. *IEEE Trans. Neural Netw. Learn. Syst.* **2023**, *34*, 4488–4498. [CrossRef] [PubMed]
12. Sun, N.; Yang, T.; Chen, H.; Fang, Y. Dynamic feedback antiswing control of shipboard cranes without velocity measurement: Theory and hardware experiments. *IEEE Trans. Ind. Inform.* **2019**, *15*, 2879–2891. [CrossRef]
13. Yang, T.; Sun, N.; Chen, H.; Fang, Y. Neural network-based adaptive antiswing control of an underactuated ship-mounted crane with roll motions and input dead zones. *IEEE Trans. Neural Netw. Learn. Syst.* **2020**, *31*, 901–914. [CrossRef] [PubMed]
14. Tuan, L.A.; Ha, Q.; Van Trieu, P. Observer-based nonlinear robust control of floating container cranes subject to output hysteresis. *J. Dyn. Syst. Meas. Control* **2019**, *141*, 111002. [CrossRef]
15. Zhai, M.; Yang, T.; Sun, N.; Fang, Y. Observer-based adaptive fuzzy control of underactuated offshore cranes for cargo stabilization with respect to ship decks. *Mech. Mach. Theory* **2022**, *175*, 104927. [CrossRef]
16. Han, J. From PID to active disturbance rejection control. *IEEE Trans. Ind. Electron.* **2009**, *56*, 900–906. [CrossRef]
17. Gao, Z. Scaling and bandwidth-parameterization based controller tuning. In Proceedings of the American Control Conference, Denver, CO, USA, 4–6 June 2003; pp. 4989–4996. [CrossRef]

18. Lu, B.; Fang, Y.; Lin, J.; Hao, Y.; Cao, H. Nonlinear antiswing control for offshore boom cranes subject to ship roll and heave disturbances. *Autom. Constr.* **2021**, *131*, 103843. [CrossRef]
19. Li, Z.; Chen, H.; Che, L. Antiswing control of offshore cranes under ship rolling disturbances: An active disturbance rejection control based approach. *Nonlinear Dyn.* **2024**, *112*, 21097–21116. [CrossRef]
20. Li, F.; Wu, X.; Zhang, Y.; Ke, L. Model-independent regulation control for offshore cranes based on finite time disturbance observer. *Nonlinear Dyn.* **2025**, *113*, 23069–23081. [CrossRef]
21. Sun, C.; Liu, C.; Feng, X.; Jiao, X. Visual servoing of flying robot based on fuzzy adaptive linear active disturbance rejection control. *IEEE Trans. Circuits Syst. II Exp. Briefs* **2021**, *68*, 2558–2562. [CrossRef]
22. Phan, V.D.; Le, V.C.; Dinh, V.N.; Duong, D.T.; Ho, S.P. A novel adaptive terminal sliding mode tracking control of engine electronic throttle system using an enhanced observer under composite disturbances. *Sensors* **2026**, *26*, 6070. [CrossRef] [PubMed]
23. Ortiz Hernández, J.C.; Rosas Almeida, D.I.; González Solís, E.V. Overcoming inclined surface challenges in Mecanum-wheeled robots using active disturbance rejection control. *Control Theory Technol.* **2025**, *23*, 437–453. [CrossRef]

Disclaimer/Publisher's Note: The statements, opinions and data contained in all publications are solely those of the individual author(s) and contributor(s) and not of MDPI and/or the editor(s). MDPI and/or the editor(s) disclaim responsibility for any injury to people or property resulting from any ideas, methods, instructions or products referred to in the content.